Robust Multiple Model Predictive Control for Ascent Trajectory Tracking of Aerospace Vehicles

RUI CAO
YANBIN LIU
Nanjing University of Aeronautics and Astronautics, Nanjing, China

YUPING LU
Nanjing University of Aeronautics and Astronautics, Nanjing, China

For aerospace vehicles with uncertainty, strong nonlinearity, and high-performance requirements, the model predictive control (MPC) method has attracted many researchers' attention with its unique advantages. Although this method has a good effect, it is computationally expensive, especially for the nonlinear MPC. In addition, it cannot guarantee the stability performance requirements and limited flexibility in dealing with large initial errors. To overcome these limitations, this article is implemented to obtain a control scheme that can handle uncertainty, initial deviation, and has less online calculation. To ensure the stability requirements, the guardian maps (GM) theory is combined with multimodel predictive control, and a switching rule based on GM is proposed. Then, fully considering the characteristics of linear matrix inequalities used, the idea of "offline design and online optimization" is adopted to solve the control law, which reduces the burden of online computing. Furthermore, in the case of large initial errors, a transient trajectory design method is established to reconstruct the trajectory online, and to modify the tracking command. Simulation results verify the effectiveness of the designed control scheme.

Manuscript received September 23, 2020; revised June 14, 2021 and September 11, 2021; released for publication September 11, 2021. Date of publication October 1, 2021; date of current version April 12, 2022.

DOI. No. 10.1109/TAES.2021.3117058

Refereeing of this contribution was handled by R. Bhattacharya.

This work was supported in part by the National Natural Science Foundation of China under Grant 11572149, in part by Six Talent Peaks Project in Jiangsu Province of China under Grant KTHY-025, and in part by Natural Science Foundation of Jiangsu Province of China under Grant BK20200437.

Authors' addresses: Rui Cao and Yanbin Liu are with the College of Automation Engineering, Nanjing University of Aeronautics and Astronautics (NUAA), Nanjing 210016, China, E-mail: (stdio@nuaa.edu.cn; nuaa_liuyanbin@139.com), Yuping Lu is with the College of Astronautics, Nanjing University of Aeronautics and Astronautics, Nanjing 210016, China, E-mail: (yplac@nuaa.edu.cn). *(Corresponding author: Yanbin Liu.)*

0018-9251 © 2021 IEEE

NOMENCLATURE

x	Horizontal displacement.
h	Altitude.
V	Speed.
γ	Flight-path angle.
α	Angle of attack (AOA).
q	Pitch angle rate.
$m_{\_\text{vehicle}}$	Vehicle mass.
D_{vehicle}	Drag force.
L_{vehicle}	Lift force.
M_y	Pitch moment.
I_y	Inertia moment.
T	Thrust.
δ_e	Elevon deflection.
ϕ	Fuel equivalent ratio (FER).
Γ	Finite-dimensional linear system.
Q	Scheduling variable $Q = [V, h]$.
$\tilde{\delta}$	Gap metric.
Φ	Flight envelope.
ω	Uncertainty caused by aerodynamic parameters.
N_p	Predictive horizon.
$\boldsymbol{X}_f$	The terminal constraint set.
n_u	Input dimension.
n_k	Number of subenvelopes.
n	State dimension.
Ω	Stability domain.
Φ_m	The maximum controllable interval under the control parameter K_m.
K_m	Control law of the mth subsystem.
$\lambda(\boldsymbol{A})$	Eigenvalues of matrix $\boldsymbol{A}$.
$\mathbb{R}$	Real number set.
$\mathbb{C}$	Complex set.

I. INTRODUCTION

In recent years, aerospace vehicles (ASVs) have developed rapidly due to their huge economic and military value, and have become an indispensable research direction in the aerospace field [1], [2]. The wide range of velocity and altitude of the ASV makes its dynamic characteristics change significantly within the flight envelope [2], and there are parameter uncertainties due to the modeling error or the uncertain environment. Therefore, accurate tracking of ascent trajectories has become one of the most critical issues for ASVs. Trajectory tracking is a crucial type of motion control problem. Compared with path tracking, the biggest difference is that the reference path curve is related to both time and space, that is, an ASV is required to reach a preset reference point within a specified time. In addition, because of the strong coupling between propulsion and aerodynamic effects, the motion equations in the large envelope flight are more complicated than in the cruising flight around a certain flight point [3]. Moreover, the slight deviations may be amplified in supersonic or hypersonic flight, resulting in undesirable tracking results. Thus, the controller designed for ASVs needs the characteristics of fast response (the control law is solved quickly and can be updated before the change of ASV motion characteristics) and high precision.

Authorized licensed use limited to: NANJING UNIVERSITY OF AERONAUTICS AND ASTRONAUTICS. Downloaded on April 15,2022 at 03:18:40 UTC from IEEE Xplore. Restrictions apply.

In addition, the actuator margin, coupled with the complex environment and possible initial deviation, imposes the higher requirements for the controller. Consequently, the issues such as constraint, nonlinearity, uncertainty, initial deviation, and time varying still need to be resolved when designing a controller for the ASV.

Some work has addressed the large-scale tracking problem of ASVs. The dynamic inversion control theory was applied to design a tracking controller for ASVs in [4], but this theory relied on the exact system model. Xu *et al.* [5] presented a robust adaptive sliding mode control strategy for the tracking control problem of ASV longitudinal dynamics. In addition, more and more researchers applied nonlinear model predictive control (NMPC) to aerospace vehicles. For example, [6]–[8] used the NMPC method to design the tracking control law. Other control strategies, including fuzzy logic and neural network, can be found in [9] and [10]. For the ASV, a highly nonlinear object, it promotes people's interest in nonlinear model predictive control [6]–[8]. However, there are some theoretical or technical problems in the implementation of NMPC, which are mainly manifested in the following ways:

1) it is very difficult to establish a global exact model of the ASV nonlinear system;
2) the core of NMPC is to solve constrained nonlinear optimization problems online, but the existing methods are difficult to be applied in practice due to its large calculation and slow solution speed [11].

A feasible way to deal with nonlinear systems with wide operating ranges is the multimodel predictive control (MMPC) method. The multimodel method utilizes a linear model set to approximate the nonlinear system for handling the nonlinearity and wide operating ranges [12]–[14]. This method is inspired by two aspects: one is many dynamical systems are parameter dependent in nature; the other is motivated by the common strategy of decomposing a problem into simple subproblems. Thus, compared with NMPC, the competitive edges of the MMPC method are as follows:

1) The model structure is simple.
2) The linear controller can be used for the local model and is easy to design.
3) The inequality constraints can be systematically dealt with when designing the local controller.

A nonfragile output tracking control scheme for the ASV was presented based on a linear variable parameter (LPV) model in [15]. Tao *et al.* [16] established an LPV model for hypersonic vehicles and designed a multimodel predictive controller. In [17], a fuzzy MMPC was presented and applied to the two-tank system. Besides, the MMPC method is also used in other applications, such as path following of 4WID autonomous vehicles, UAV, reactor temperature control system, stirred tank reactor, etc. [18]–[21].

Based on the aforementioned researches, considering the disturbance and uncertainty of the actual system, we combine robust model predictive control (RMPC) with multiple models, proposing a robust multimodel predictive control (RMMPC) strategy. There are two typical design schemes for RMPC. One is the single Lyapunov model predictive control (SL-RMPC) method proposed by Lee *et al.* [22]. The SL-RMPC method designs a series of feedback control laws only on the basis of a single Lyapunov function. The other is the parameter-dependent Lyapunov model prediction (PDL-RMPC) method proposed in [23], which designs Lyapunov functions for different vertices of the polytope model. This work is based on the PDL-RMPC theory to design RMMPC. However, for this RMMPC strategy, its control performance and computational complexity put forward contradictory requirements on the controller design. It is a difficult problem that designs an RMMPC strategy effectively resolves the conflicts between different performances to obtain low computational complexity and good control behavior at the same time.

To handle the contradiction between the aforementioned multiple performances, and the ASV tracking problems with model uncertainty and initial deviation, we carry out the research work in this article and propose a new trajectory tracking control (TRT) scheme. This scheme can be easily implemented in practical applications and has small online computation compared to [6] and [23]. Compared with the passive switching rule in [16], it can realize the active switching between models to guarantee the stability of the whole system. And compared with [15] and [19], it has the ability to adjust the tracked trajectory in real-time, and further expands the feasible domain of control. The main contributions are as follows:

1) Aiming at the problem of approximating nonlinear systems with the linear model set in the global range, a gap-metric-based linear model construction algorithm is proposed to obtain a complete and nonredundant linear model set.
2) To solve the conflicting requirement issue between computational complexity and control performance, a robust comprehensive design method is proposed based on the idea of "offline design and online comprehensive optimization."
3) Considering the switching stability between subprediction controllers, a switching strategy based on guardian maps (GM) is presented. Furthermore, we combine this switching rule with the robust comprehensive design method to establish an RMMPC strategy to ensure the stability of the whole closed-loop system.
4) A new TRT scheme has been developed to make it possible to accurately reach the target point within a specific period when the parameters are uncertain and the initial deviation is large. The TRT scheme is composed of the tracking command correction module and the RMMPC strategy. The tracking command correction module can adjust the reference trajectory online to avoid the saturation of the actuator and expand the initial feasible area.

The rest of this article is organized as follows. Section II focuses on the problem formulation and analysis of the ASV

Authorized licensed use limited to: NANJING UNIVERSITY OF AERONAUTICS AND ASTRONAUTICS. Downloaded on April 15,2022 at 03:18:40 UTC from IEEE Xplore. Restrictions apply.

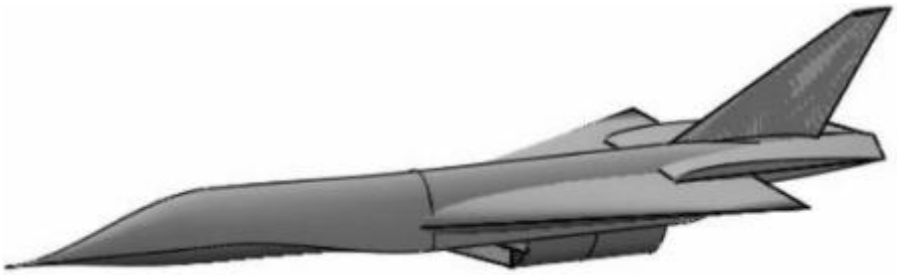

Fig. 1. GHAME vehicle configuration (established with OPenVSP software).

model. In Section III, a piecewise polytopic model of the ASV is established. Section IV gives the detailed steps to construct the TRT scheme, as well as related theorems and proofs. To verify the control performance, the simulations results are described in Section V. Finally, Section VI concludes this article.

II. PROBLEM FORMULATION

A. Longitudinal Dynamic Model of the ASV

In the wind coordinate frame, the longitudinal motion of the ASV is considered as [24]

$$\begin{cases} \dot{x} = V\cos\gamma \\ \dot{h} = V\sin\gamma \\ \dot{V} = \frac{T\cos\alpha - D_{\text{vehicle}}}{m_{\text{\_vehicle}}} - \frac{\mu_g \sin\gamma}{r_g^2} \\ \dot{\gamma} = \frac{T\sin\alpha + L_{\text{vehicle}}}{m_{\text{\_vehicle}} V} - \frac{\left(\mu_g - V^2 r_g\right)\cos\gamma}{V r_g^2} \\ \dot{\alpha} = q - \dot{\gamma} \\ \dot{q} = M_y / I_y \\ \dot{m}_{\text{\_vehicle}} = \frac{-T}{g_0 I_{sp}} \end{cases} \tag{1}$$

where $\dot{m}_{\text{\_vehicle}}$ is the fuel mass flow rate; g_0 is the gravitational acceleration of earth surface; I_{sp} represents the specific impulse; μ_g indicates the gravitational constant; and r_g denotes the earth radius.

The generic hypersonic aerodynamics model example (GHAME) vehicle [25] is adopted as an example of ASVs, and used for subsequent analysis and simulations (the configuration is shown in Fig. 1). The drag force D_{vehicle}, lift force L_{vehicle}, and pitch moment M_y of GHAME are as following:

$$\begin{aligned} &D_{\text{vehicle}} = \bar{q} S_{\text{ref}} C_D(\alpha, V), L_{\text{vehicle}} = \bar{q} S_{\text{ref}} C_L(\alpha, V, \delta_e), \\ &M_y = \bar{q} c S_{\text{ref}} C_M(\alpha, V, \delta_e) \end{aligned} \tag{2}$$

where S_{ref} represents the wing area; c denotes mean aerodynamic chord; $\bar{q}$ indicates the dynamic pressure; and C_D, C_L, and C_M are the aerodynamic coefficients.

GHAME adopts the turbine-based-combined cycle (TBCC) engine layout [26], its thrust model expression is as follows:

$$T = 0.029\phi I_{sp}(Ma, \phi)\rho g_0 V C_t(Ma, \alpha) c_a \tag{3}$$

where Ma is Mach number, C_t denotes the capture-area coefficient, ρ is the atmospheric density, and $c_a = 34.68\text{m}^2$ is the inlet capture area. The aerodynamic and propulsion coefficients in (2) and (3) can refer to [26] and [27].

B. Ascent Phase Tracking Problem

The TBCC engine control and flight control of ASVs are independent of each other. In the process of the ascent trajectory tracking, ASVs need to reach the target point accurately within the specified time to ensure the cooperative work between flight control and engine control. In addition, from (2) and (3), it can be seen that the aerodynamic and propulsion parameters of GHAME will change with the current state, that is, the system (1) is highly nonlinear. Moreover, under the high-speed flight condition, the aerodynamic parameter uncertainty would cause significant alterations of state variables. Therefore, the tracking controller design of the ASV is mainly confronted with the following four problems.

1) How to establish a linear model set that can approximate the original nonlinear system in the working range, and how to ensure the switching stability between models.
2) How to solve the influence of aerodynamic uncertainty. The complex unknown environment and the strong coupling caused by unique layout of the ASV, which make the ASV strong aerodynamic uncertainty.
3) How to eliminate the negative effects of initial deviation on tracking control. Due to the supersonic or hypersonic flight and small control margin, a slight deviation could cause control saturation, thereby, generating the poor tracking results.
4) How to reduce the online computation amount of the MPC method to satisfy the real-time requirements.

To solve these tracking control problems in the ascent phase, a novel TRT scheme is developed. The scheme can design the control law in the case of aerodynamic parameter uncertainty and initial deviation, so as to accurately track the reference trajectory within the control constraints. Before the control scheme is proposed, the nonlinear model of the ASV is processed to obtain the approximate linear model set within the operating range.

Authorized licensed use limited to: NANJING UNIVERSITY OF AERONAUTICS AND ASTRONAUTICS. Downloaded on April 15,2022 at 03:18:40 UTC from IEEE Xplore. Restrictions apply.

III. MODEL MANIPULATION

Set $\boldsymbol{X} = [x, h, V, \gamma, \alpha, q, m_{\_\text{vehicle}}]^{\mathrm{T}}$, $\boldsymbol{u} = [\delta_e, \phi]^{\mathrm{T}}$, (1) is converted to

$$\dot{\boldsymbol{X}} = f(\boldsymbol{X}, \boldsymbol{u}) \tag{4}$$

where $f(\cdot)$ represents the nonlinear kinematic equation of the ASV shown in (1). The system input constraint is shown as follow:

$$\left\|\boldsymbol{u}_{i_u}\right\| \leqslant \boldsymbol{u}_{i_u,\max},\ i_u = 1, 2, \ldots, n_u \tag{5}$$

where the subscript i_u represents the i_uth control input variable. $\boldsymbol{u}_{i_u,\max}$ denotes the upper bound of the amplitude of the i_uth control input.

A. Piecewise Linearization Based on Gap Metric

In order to design a TRT scheme for the ascent trajectory tracking, the first is to select the reasonable linear model set to accurately describe the dynamic response of the ASV during the flight. The common method of constructing a linear model set is to repeatedly experiment, that is, a set of linear models is selected in advance, and then, they are repeatedly replaced or reduced according to the simulation results, until a satisfactory performance is obtained [16]. This strategy usually has model redundancy and is time-consuming. Therefore, the gap metric method is introduced into the multimodel approach to handle the aforementioned problem, which can measure the distance between two linear systems [28].

The gap value between two systems Γ_1 and Γ_2 is expressed as

$$\tilde{\delta}(\Gamma_1, \Gamma_2) = \max\left\{\overline{\delta}(\Gamma_1, \Gamma_2), \overline{\delta}(\Gamma_2, \Gamma_1)\right\} \tag{6}$$

where $\tilde{\delta} \in (0, 1)$, and the similarity of these two systems is inversely proportional to $\tilde{\delta}$. The expression of $\overline{\delta}(\Gamma_i, \Gamma_j)$ is as follows:

$$\overline{\delta}\left(\Gamma_i, \Gamma_j\right) = \inf_{\Xi \in H_\infty} \left\| \begin{pmatrix} D_i \\ N_i \end{pmatrix} - \begin{pmatrix} D_j \\ N_j \end{pmatrix} \Xi \right\|_\infty,\ i, j \in \{1, 2\},\ i \neq j \tag{7}$$

where D and N represent the right and left coprime factors, $\Gamma = ND^{-1}$. Set $\Lambda = \begin{pmatrix} D \\ N \end{pmatrix}$, and $\Xi \in H_\infty$ (represents the Hilbert space), which satisfies the following inequality:

$$\left\|\left(I - \Lambda\overline{\Lambda}\right)\Lambda\right\| = \inf_{\Xi \in H_\infty} \left\|\hat{\Lambda} - \hat{\Lambda}\Xi\right\|_\infty$$

where $\overline{\Lambda}$ and $\hat{\Lambda}$ are the conjugate matrix and transfer matrix of Λ, respectively.

Since the aerodynamic model of the ASV varies significantly with velocity and height, they are selected as the scheduling variables $Q = [V, h]$, to establish a piecewise linear model that reflects the nonlinear characteristics of the ASV in the flight envelope. Denote the flight envelope as $\Phi = [V_{\min}, V_{\max}] \times [h_{\min}, h_{\max}]$. Next, we will describe the process of building a piecewise linear model based on the gap metric theory.

Algorithm 1: Linear Model Construction Based on Gap Metric.

Step 1 Divide the flight envelope Φ evenly via Δv and Δh to obtain $N_\Phi \times Q_\Phi$ state point $N_\Phi = (V_{\max} - V_{\min})/\Delta v + 1$, $Q_\Phi = (h_{\max} - h_{\min})/\Delta h + 1$.

Step 2 Obtain the equilibrium points near $N_\Phi \times Q_\Phi$ state points, and use the Jacobi linearization method to establish the linear model $\Gamma_{1,2\ldots,N_\Phi \times Q_\Phi}$.

Step 3 Prescribe a distance level λ. Calculate the gap metric values between equilibrium points. If the following inequalities are satisfied, the corresponding velocity and height are the boundary values of subenvelope.

$$\sum_{h=h_{i,\min}}^{h_{i,\max}} \tilde{\delta} \geqslant \lambda,\quad \sum_{V=V_{i,\min}}^{V_{i,\max}} \tilde{\delta} \geqslant \lambda$$

Finally, Φ is divided into n_k subenvelopes, denoted as $\phi_i = [V_{i,\min}, V_{i,\max}] \times [h_{i,\min}, h_{i,\max}]$, $i = 1, 2, \ldots, n_k$ and satisfies $\phi_i \in \Phi$, $\phi_1 \cup \phi_2 \cup \cdots \cup \phi_{n_k} = \Phi$.

Step 4 Get the nominal point Υ_m of each subenvelope, $m \in [1, 2, \ldots, n_k]$. If the sum $\tilde{\delta}_s(\Upsilon_m)$ of the gap metric between Υ_m and other state points Υ_a in the subenvelope ϕ_m satisfies

$$\tilde{\delta}_s(\Upsilon_m) = \min_{\Upsilon_m \in \phi_m} \left[\sum_{\Upsilon_a \in \phi_m} \tilde{\delta}\left(\Gamma(\Upsilon_m), \Gamma(\Upsilon_a)\right) \right]$$

then Υ_m is called the nominal point. The n_k nominal points are obtained, defined as $\Upsilon_{1,2,\ldots,nk}$.

Step 5 Linearization of (4) around nominal point Υ_m and discretization, the following linear model Γ_m is obtained:

$$\begin{cases} \boldsymbol{X}(k+1) = \boldsymbol{A}_m\boldsymbol{X}(k) + \boldsymbol{B}_m\boldsymbol{u}(k) \\ \boldsymbol{y}(k) = \boldsymbol{C}\boldsymbol{X}(k) \end{cases},\ Q(k) \in \phi_m \tag{8}$$

where $Q(k) \in \phi_m$ indicates that ASV is in the mth subinterval at time k. $\boldsymbol{A}_m$, $\boldsymbol{B}_m$, and $\boldsymbol{C}$ are the state-space matrices. $\boldsymbol{X}(k)$ and $\boldsymbol{u}(k)$ represent the system state and input at the sampling time k.

The linear model (8) is an approximation of the longitudinal dynamic model (1) in the subregion ϕ_m. If combine the linear model of each subregion into a piecewise linear system, we have

$$\boldsymbol{\Gamma} : \left\{\Gamma_1, \Gamma_2, \ldots, \Gamma_m, \ldots, \Gamma_{n_k}\right\}$$
$$\Gamma_m = \begin{cases} \boldsymbol{X}(k+1) = \boldsymbol{A}_m\boldsymbol{X}(k) + \boldsymbol{B}_m\boldsymbol{u}(k) \\ \boldsymbol{y}(k) = \boldsymbol{C}\boldsymbol{X}(k) \end{cases},\ Q(k) \in \phi_m \tag{9}$$

where the system output is $\boldsymbol{y}(t) \triangleq [x(t), h(t), V(t), \gamma(t), \alpha(t), q(t)]^{\mathrm{T}}$, and $\boldsymbol{C} = [\boldsymbol{I}_{6\times 6}, 0]$. The piecewise linear system (9) can be regarded as a linear approximation of the nonlinear system (1) in the

Authorized licensed use limited to: NANJING UNIVERSITY OF AERONAUTICS AND ASTRONAUTICS. Downloaded on April 15,2022 at 03:18:40 UTC from IEEE Xplore. Restrictions apply.

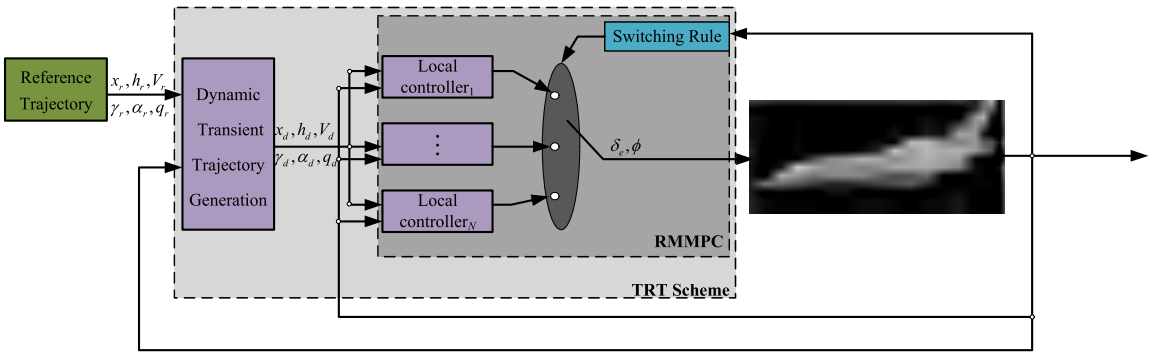

Fig. 2. Framework of the TRT control scheme.

global flight envelope Φ. Based on the system (9), a linear controller can be designed for each linear model, which is called the local controller.

B. Piecewise Polytopic Model

Considering the aerodynamic uncertainty of the ASV, (9) can be written as

$$\begin{cases} \boldsymbol{X}(k+1) = \boldsymbol{A}_m(\omega(k))\boldsymbol{X}(k) + \boldsymbol{B}_m(\omega(k))\boldsymbol{u}(k) \\ \boldsymbol{y}(k) = \boldsymbol{C}\boldsymbol{X}(k) \end{cases}, \quad Q(k) \in \phi_m. \tag{10}$$

Since this article focuses on the tracking control, it is assumed that the reference trajectory considering constraints, such as state and dynamic pressure, is predesigned by some optimization methods [29]–[33] and described by $\boldsymbol{y}_r(t) = [x_r(t), h_r(t), V_r(t), \gamma_r(t), \alpha_r(t), q_r(t)]$, and its time range is $t \in [t_0, t_f]$.

The tracking error is defined as $\boldsymbol{e}(k) = \boldsymbol{y}(k) - \boldsymbol{y}_r(k)$, and the system (10) is extended to

$$\begin{cases} \tilde{\boldsymbol{X}}(k+1) = \tilde{\boldsymbol{A}}_m(\omega(k))\tilde{\boldsymbol{X}}(k) + \tilde{\boldsymbol{B}}_m(\omega(k))\boldsymbol{u}(k) + \tilde{\boldsymbol{G}}\boldsymbol{y}_r(k) \\ \boldsymbol{y}(k) = \tilde{\boldsymbol{C}}\tilde{\boldsymbol{X}}(k) \end{cases}, \quad Q(k) \in \phi_m \tag{11}$$

where

$$\tilde{\boldsymbol{X}}(k) \triangleq \begin{bmatrix} \boldsymbol{X}(k) \\ \boldsymbol{e}(k) \end{bmatrix}, \tilde{\boldsymbol{A}}_m(\omega(k)) = \begin{bmatrix} \boldsymbol{A}_m(\omega(k)) & 0 \\ \boldsymbol{C}\boldsymbol{A}_m(\omega(k)) & 0 \end{bmatrix}$$
$$\tilde{\boldsymbol{B}}_m(\omega(k)) = \begin{bmatrix} \boldsymbol{B}_m(\omega(k)) \\ \boldsymbol{C}\boldsymbol{B}_m(\omega(k)) \end{bmatrix}, \tilde{\boldsymbol{G}} = \begin{bmatrix} 0 \\ -\boldsymbol{I} \end{bmatrix}, \tilde{\boldsymbol{C}} = \begin{bmatrix} \boldsymbol{C} & 0 \end{bmatrix}.$$

Since $\omega(k)$ is bounded in (11), the system matrix $[\tilde{\boldsymbol{A}}_m(\omega(k)), \tilde{\boldsymbol{B}}_m(\omega(k))]$ of mth subinterval is also constrained. Then, tensor product modeling [34] is performed on uncertain discrete subsystems (11) to obtain the polytopic model

$$\left[\tilde{\boldsymbol{A}}_m(\omega(k)), \tilde{\boldsymbol{B}}_m(\omega(k))\right] = \sum_{j=1}^{L} \sigma_{mj}\left[\tilde{\boldsymbol{A}}_{mj}, \tilde{\boldsymbol{B}}_{mj}\right] \tag{12}$$

where L is the number of vertex matrices, and $\tilde{\boldsymbol{A}}_{mj}$ and $\tilde{\boldsymbol{B}}_{mj}$ represent the vertex matrices. σ_{mj} denotes the weight function, which satisfies

$$\begin{cases} \sigma_{mj} \in (0, 1] \\ \sum_{j=1}^{L} \sigma_{mj} = 1. \end{cases} \tag{13}$$

The ranges of $\tilde{\boldsymbol{A}}_m(\omega(k))$ and $\tilde{\boldsymbol{B}}_m(\omega(k))$ are in convex hull $\{[\tilde{\boldsymbol{A}}_{m1}|\tilde{\boldsymbol{B}}_{m1}], [\tilde{\boldsymbol{A}}_{m2}|\tilde{\boldsymbol{B}}_{m2}], \ldots, [\tilde{\boldsymbol{A}}_{mL}|\tilde{\boldsymbol{B}}_{mL}]\}$. Therefore, if one controller can stabilize the entire convex hull, the robust stability of the uncertain system can be guaranteed.

IV. TRT SCHEME

The TRT scheme of the ASV is made up of tracking command correction module and RMMPC strategy, as shown in Fig. 2. The tracking command correction module is applied to modify the reference trajectory online at first. Then, the RMMPC strategy is used to design the controller to automatically adjust the elevator angle and fuel equivalence ratio so that the ASV can track the corrected trajectory.

A. RMMPC Strategy Based on GM

In this section, the detailed steps to design the RMMPC strategy are given. According to Fig. 2, the RMMPC strategy consists of two parts: one is the local controllers, which ensures the local stability of working point, the other is the switching rules to guarantee the switching stability, thereby making the whole closed-loop system stable.

Assuming that the current operating point k corresponds to the mth subsystem, the following feedback tracking controller is considered:

$$\boldsymbol{u}(k+i) = \boldsymbol{K}_m\tilde{\boldsymbol{X}}(k+i|k) \tag{14}$$

then apply the feedback control (14) to the mth subsystem, we get

$$\begin{cases} \tilde{\boldsymbol{X}}(k+1) = \left(\tilde{\boldsymbol{A}}_m(\omega(k)) + \tilde{\boldsymbol{B}}_m(\omega(k))\boldsymbol{K}_m\right)\tilde{\boldsymbol{X}}(k) + \tilde{\boldsymbol{G}}\boldsymbol{y}_r(k) \\ \boldsymbol{y}(k) = \tilde{\boldsymbol{C}}\tilde{\boldsymbol{X}}(k) \end{cases} \tag{15}$$

where $Q(k) \in \phi_m$, $m \in [1, 2, \ldots, n_k]$.

To guarantee the local stability, we take the local controller as a receding horizon scheme with a finite horizon objective function (16). In (16), i starts from 1 because $\tilde{\boldsymbol{X}}$ (k) is already known, so it does not need to be regarded as

Authorized licensed use limited to: NANJING UNIVERSITY OF AERONAUTICS AND ASTRONAUTICS. Downloaded on April 15,2022 at 03:18:40 UTC from IEEE Xplore. Restrictions apply.

optimization information.

$$J(k) = \|\boldsymbol{u}\|_{\bar{\boldsymbol{R}}}^2 + \sum_{i=1}^{N_p-1} \left(\|\boldsymbol{u}(k+i|k)\|_{\bar{\boldsymbol{R}}}^2 + \left\|\tilde{\boldsymbol{X}}(k+i|k)\right\|_{\bar{\boldsymbol{Q}}}^2 \right) + E\left(\tilde{\boldsymbol{X}}\left(k+N_p|k\right)\right) \tag{16}$$

$$\bar{\boldsymbol{Q}} = \begin{bmatrix} \boldsymbol{0}_{n\times n} & \boldsymbol{0} \\ \boldsymbol{0} & \boldsymbol{Q}_e \end{bmatrix}$$

where $\|\boldsymbol{u}\|_{\bar{\boldsymbol{R}}}^2 = \boldsymbol{u}^{\mathrm{T}}(k)\bar{\boldsymbol{R}}\boldsymbol{u}(k)$. $\boldsymbol{Q}_e = {\boldsymbol{Q}_e}^{\mathrm{T}} > 0$, $\bar{\boldsymbol{R}} = \bar{\boldsymbol{R}}^{\mathrm{T}} > 0$ represent the weighting matrices of the state and control input, respectively. $E(\tilde{\boldsymbol{X}}(k+N_p|k)) = \|\tilde{\boldsymbol{X}}(k+N_p|k)\|_{\boldsymbol{G}_e}^2$ is the terminal penalty term [35], which indicates $E(\tilde{\boldsymbol{X}}(k+N_p|k)) \in \boldsymbol{X}_f$. $\boldsymbol{X}_f$ denotes the terminal constraint set, and ${\boldsymbol{X}_f}^{\mathrm{T}}\boldsymbol{X}_f = \ell$, $0 \in \boldsymbol{X}_f$. Then, we can get

$$\left\|\tilde{\boldsymbol{X}}\left(k+N_p|k\right)\right\|_{\boldsymbol{G}_e}^2 \leqslant \left\|\boldsymbol{X}_f\right\|^2 = \ell \qquad \boldsymbol{G}_e = \begin{bmatrix} \boldsymbol{0}_{n\times n} & \boldsymbol{0} \\ \boldsymbol{0} & \boldsymbol{I} \end{bmatrix}. \tag{17}$$

1) *Design of the Local Controller:* The analysis conditions of the output tracking control performance for the closed-loop subsystem (15) are given in the following lemmas and theorems.

The Lyapunov function of the jth vertex of the polytopic model is set to

$$V\left(\tilde{\boldsymbol{X}}(k+i|k), j\right) = \tilde{\boldsymbol{X}}(k+i|k)^{\mathrm{T}}\boldsymbol{P}_j\tilde{\boldsymbol{X}}(k+i|k) \ \left(0 \leqslant i \leqslant N_p\right)$$

where $\tilde{\boldsymbol{X}}(k+i|k)$ is the predictive state at time $k+i$ based on the state at time k, $\boldsymbol{P}_j$ is the positive definite matrix corresponding to the jth vertex of the polytopic model.

The current operating point k corresponds to the mth subsystem. Then, the Lyapunov function of the mth subsystem is as follows:

$$\begin{aligned} V(\tilde{\boldsymbol{X}}(k+i|k)) &= \sum_{j=1}^{L} \sigma_{mj} V(\tilde{\boldsymbol{X}}(k+i|k), j) \\ &= \tilde{\boldsymbol{X}}(k+i|k)^{\mathrm{T}} \left[\sum_{j=1}^{L} \sigma_{mj}\boldsymbol{P}_j\right] \tilde{\boldsymbol{X}}(k+i|k) \\ &\triangleq \tilde{\boldsymbol{X}}(k+i|k)^{\mathrm{T}}\hat{\boldsymbol{P}}\tilde{\boldsymbol{X}}(k+i|k) \end{aligned} \tag{18}$$

where $\hat{\boldsymbol{P}} = \sum_{j=1}^{L}\sigma_{mj}\boldsymbol{P}_j$, $\sum_{j=1}^{L}\sigma_{mj} = 1$.

According to [23], if the design requirement (19) is met, the system has robust stability under control input $\boldsymbol{u}(k+i|k)$.

$$\begin{aligned} &V\left(\tilde{\boldsymbol{X}}(k+i+1|k)\right) - V\left(\tilde{\boldsymbol{X}}(k+i|k)\right) \\ &< -\tilde{\boldsymbol{X}}(k+i|k)^{\mathrm{T}}\bar{\boldsymbol{Q}}\tilde{\boldsymbol{X}}(k+i|k) - \boldsymbol{u}(k+i|k)^{\mathrm{T}}\bar{\boldsymbol{R}}\boldsymbol{u}(k+i|k) \\ &\forall\left[\tilde{\boldsymbol{A}}_m(\omega(k))\,|\tilde{\boldsymbol{B}}_m(\omega(k))\right] \in \Theta_m,\ m \in [1,2,\ldots,n_k] \end{aligned} \tag{19}$$

where $\Theta_m := \{[\tilde{\boldsymbol{A}}_{m1}|\tilde{\boldsymbol{B}}_{m1}], [\tilde{\boldsymbol{A}}_{m2}|\tilde{\boldsymbol{B}}_{m2}], \ldots, [\tilde{\boldsymbol{A}}_{mL}|\tilde{\boldsymbol{B}}_{mL}]\}$.

The following lemma gives the condition to ensure the robust stability of closed-loop subsystems.

LEMMA 1 There exists a state feedback control law $\boldsymbol{u}(k+i) = \boldsymbol{K}_m\tilde{\boldsymbol{X}}(k+i|k)$, $i \geqslant 0$ that makes the closed-loop subsystem (15) satisfy the performance constraint (19) if there are L symmetric matrices $\boldsymbol{Q}_j (j = 1, \ldots, L)$, a pair of matrices $\{\boldsymbol{G}, \boldsymbol{Y}\}$ and a scalar $\delta \geqslant 0$, satisfying the following linear matrix inequality (LMI):

$$\begin{bmatrix} \boldsymbol{G}^{\mathrm{T}} + \boldsymbol{G} - \boldsymbol{Q}_j & * & * & * \\ \tilde{\boldsymbol{A}}_{mj}\boldsymbol{G} + \tilde{\boldsymbol{B}}_{mj}\boldsymbol{Y} & \boldsymbol{Q}_j & * & * \\ \bar{\boldsymbol{Q}}^{1/2}\boldsymbol{G} & \delta\tilde{\boldsymbol{G}}^{\mathrm{T}} & \delta\boldsymbol{I} & * \\ \bar{\boldsymbol{R}}^{1/2}\boldsymbol{Y} & 0 & 0 & \delta\boldsymbol{I} \end{bmatrix} > 0,\ j = 1, 2, \ldots, L. \tag{20}$$

PROOF Based on $\boldsymbol{u}(k+i) = \boldsymbol{K}_m\tilde{\boldsymbol{X}}(k+i|k)$, (15), and (18), the performance requirement (19) can be rewritten in the following form (21) shown at bottom of this page, where $\tilde{\boldsymbol{A}}_{mc}(\omega(k)) = \tilde{\boldsymbol{A}}_m(\omega(k)) + \tilde{\boldsymbol{B}}_m(\omega(k))\boldsymbol{K}_m$. Then, (21) is transformed into the form of the following matrix inequality, (22) shown at bottom of this page, which is equivalent to, (23) shown at bottom of next page.

$$\begin{aligned} &\left[\tilde{\boldsymbol{A}}_{mc}(\omega(k))\tilde{\boldsymbol{X}}(k+i|k) + \tilde{\boldsymbol{G}}\boldsymbol{y}_r(k)\right]^{\mathrm{T}}\hat{\boldsymbol{P}}\left[\tilde{\boldsymbol{A}}_{mc}(\omega(k))\tilde{\boldsymbol{X}}(k+i|k) + \tilde{\boldsymbol{G}}\boldsymbol{y}_r(k)\right] - \tilde{\boldsymbol{X}}(k+i|k)^{\mathrm{T}}\hat{\boldsymbol{P}}\tilde{\boldsymbol{X}}(k+i|k) \\ &< -\tilde{\boldsymbol{X}}(k+i|k)^{\mathrm{T}}\bar{\boldsymbol{Q}}\tilde{\boldsymbol{X}}(k+i|k) - \left[\boldsymbol{K}_m\tilde{\boldsymbol{X}}(k+i|k)\right]^{\mathrm{T}}\bar{\boldsymbol{R}}\left[\boldsymbol{K}_m\tilde{\boldsymbol{X}}(k+i|k)\right] \\ &\forall\left[\tilde{\boldsymbol{A}}_m(\omega(k))\,|\tilde{\boldsymbol{B}}_m(\omega(k))\right] \in \Theta_m,\ m \in [1,2,\ldots,n_k] \end{aligned} \tag{21}$$

$$\begin{aligned} &\begin{bmatrix} \tilde{\boldsymbol{X}}(k+i|k) \\ \boldsymbol{y}_r(k) \end{bmatrix}^{\mathrm{T}} \\ &\times \begin{bmatrix} \left(\tilde{\boldsymbol{A}}_m(\omega(k)) + \tilde{\boldsymbol{B}}_m(\omega(k))\boldsymbol{K}_m\right)^{\mathrm{T}}\hat{\boldsymbol{P}}\left(\tilde{\boldsymbol{A}}_m(\omega(k)) + \tilde{\boldsymbol{B}}_m(\omega(k))\boldsymbol{K}_m\right) - \hat{\boldsymbol{P}} + \bar{\boldsymbol{Q}} + {\boldsymbol{K}_m}^{\mathrm{T}}\bar{\boldsymbol{R}}\boldsymbol{K}_m & * \\ \tilde{\boldsymbol{G}}^{\mathrm{T}}\hat{\boldsymbol{P}}\left(\tilde{\boldsymbol{A}}_m(\omega(k)) + \tilde{\boldsymbol{B}}_m(\omega(k))\boldsymbol{K}_m\right) & \tilde{\boldsymbol{G}}^{\mathrm{T}}\hat{\boldsymbol{P}}\tilde{\boldsymbol{G}} \end{bmatrix} \\ &\times \begin{bmatrix} \tilde{\boldsymbol{X}}(k+i|k) \\ \boldsymbol{y}_r(k) \end{bmatrix} < 0 \end{aligned} \tag{22}$$

Authorized licensed use limited to: NANJING UNIVERSITY OF AERONAUTICS AND ASTRONAUTICS. Downloaded on April 15,2022 at 03:18:40 UTC from IEEE Xplore. Restrictions apply.

Next, (23) can be rewritten as (24) shown at bottom of this page.

By Schur complements, this is equivalent to, (25) shown at the bottom of this page. By left multiplying and right multiplying (25) by $\begin{bmatrix} \boldsymbol{I} & 0 & 0 \\ 0 & 0 & \boldsymbol{I} \\ 0 & \boldsymbol{I} & 0 \end{bmatrix}$, the following inequality can be obtained, (26) shown at the bottom of this page.

Let $\boldsymbol{P}_j = \delta \boldsymbol{Q}_j{}^{-1}$, convert $\tilde{\boldsymbol{A}}_m(\omega(k+i))$ and $\tilde{\boldsymbol{B}}_m(\omega(k+i))$ into the polytopic model (12). It can be shown, after several steps involving Schur complements and algebraic manipulation, that (26) is equivalent to

$$\begin{bmatrix} \boldsymbol{Q}_j & * & * & * \\ \left[\tilde{\boldsymbol{A}}_{mj} + \tilde{\boldsymbol{B}}_{mj}\boldsymbol{K}_m\right]\boldsymbol{Q}_j & \boldsymbol{Q}_j & * & * \\ \bar{\boldsymbol{Q}}^{1/2}\boldsymbol{Q}_j & \delta\tilde{\boldsymbol{G}}^{\mathrm{T}} & \delta\boldsymbol{I} & * \\ \bar{\boldsymbol{R}}^{1/2}\boldsymbol{K}_m\boldsymbol{Q}_j & 0 & 0 & \delta\boldsymbol{I} \end{bmatrix} > 0,\ j = 1, 2, \ldots, L. \tag{27}$$

According to the study of Oliveira *et al.* [36], it can be concluded that $\forall j \in [1, 2, \ldots, L]$, (27) holds if the following inequality is satisfied: where $\boldsymbol{G} > 0$ and $0 < \boldsymbol{G}^{\mathrm{T}} + \boldsymbol{G} - \boldsymbol{Q}_j \leqslant \boldsymbol{G}^{\mathrm{T}}\boldsymbol{Q}_j{}^{-1}\boldsymbol{G}$ [23]. Define $\boldsymbol{Y} = \boldsymbol{K}_m\boldsymbol{G}$, (28) shown at the bottom of next page, is transformed into

$$\begin{bmatrix} \boldsymbol{G}^{\mathrm{T}} + \boldsymbol{G} - \boldsymbol{Q}_j & * & * & * \\ \tilde{\boldsymbol{A}}_{mj}\boldsymbol{G} + \tilde{\boldsymbol{B}}_{mj}\boldsymbol{Y} & \boldsymbol{Q}_j & * & * \\ \bar{\boldsymbol{Q}}^{1/2}\boldsymbol{G} & \delta\tilde{\boldsymbol{G}}^{\mathrm{T}} & \delta\boldsymbol{I} & * \\ \bar{\boldsymbol{R}}^{1/2}\boldsymbol{Y} & 0 & 0 & \delta\boldsymbol{I} \end{bmatrix} > 0,\ j = 1, 2, \ldots, L.$$

Therefore, constraint (19) is satisfied, if and only if the inequality (20) holds. ■

Based on Lemma 1, the following theorem develops an LMI solution for stabilizing the uncertain subsystem and minimizing the performance index (16).

THEOREM 1 If there exist L symmetric matrices $\boldsymbol{Q}_j (j = 1, \ldots, L)$, a pair of matrices $\{\boldsymbol{G}, \boldsymbol{Y}\}$ and a scalar $\delta \geqslant 0$ satisfy constraints in (29), and the control law $\boldsymbol{u}(k+i) = \boldsymbol{K}_m\tilde{\boldsymbol{X}}(k+i|k)$ can solve the following optimization problem, (29) shown at the bottom of next page, then, under the constraints (5), the robust stability of the closed-loop subsystem (15) is guaranteed. The control law $\boldsymbol{K}_m$ is given via

$$\boldsymbol{K}_m = \boldsymbol{Y}\boldsymbol{G}^{-1}. \tag{30}$$

PROOF For the uncertain subsystem (15), its tensor product model is

$$\begin{aligned} \tilde{\boldsymbol{X}}(k+1) &= \sum_{j=1}^{L} \sigma_{mj}\tilde{\boldsymbol{A}}_{mj}\tilde{\boldsymbol{X}}(k) + \sum_{j=1}^{L} \sigma_{mj}\tilde{\boldsymbol{B}}_{mj}\boldsymbol{u}(k) + \tilde{\boldsymbol{G}}\boldsymbol{y}_r(k) \\ &s.t.\ \left\|\boldsymbol{u}_{i_u}\right\| \leqslant \boldsymbol{u}_{i_u,\max},\ i_u = 1, 2, \ldots, n_u. \end{aligned} \tag{31}$$

Derivation of robust stability of the subsystems (15) According to Lemma 1, when inequality (20) holds, the closed-loop system satisfies the requirement of the robust stability performance (19). It means that if (20) holds, the closed-loop subsystem (15) is robustly asymptotically stable.

Derivation of condition (17) According to (14) and (15) and $\boldsymbol{K}_m = \boldsymbol{Y}\boldsymbol{G}^{-1}$, the expression of the predicted state $\tilde{\boldsymbol{X}}(k+N_p|k)$ can be get as follows

$$\begin{aligned} \tilde{\boldsymbol{X}}\left(k+N_p|k\right) &= \boldsymbol{\Lambda}_m(\omega(k))\tilde{\boldsymbol{X}}(k) \\ &\quad + \boldsymbol{Z}_m(\omega(k))\boldsymbol{u}(k) + \boldsymbol{L}_m(\omega(k))\boldsymbol{y}_r(k) \\ &= \left(\boldsymbol{\Lambda}_m(\omega(k)) + \boldsymbol{Z}_m(\omega(k))\boldsymbol{Y}\boldsymbol{G}^{-1}\right)\tilde{\boldsymbol{X}}(k) \\ &\quad + \boldsymbol{L}_m(\omega(k))\boldsymbol{y}_r(k) \\ \boldsymbol{\Lambda}_m(\omega(k)) &= \tilde{\boldsymbol{A}}_m(\omega(k))^{N_p} \\ \boldsymbol{Z}_m(\omega(k)) &= \left(\tilde{\boldsymbol{A}}_m(\omega(k))^{N_p-1} + \tilde{\boldsymbol{A}}_m(\omega(k))^{N_p-2}\right. \\ &\quad \left. + \cdots + \tilde{\boldsymbol{A}}_m(\omega(k)) + \boldsymbol{I}\right)\tilde{\boldsymbol{B}}_m(\omega(k)) \\ \boldsymbol{L}_m(\omega(k)) &= \left(\tilde{\boldsymbol{A}}_m(\omega(k))^{N_p-1} + \tilde{\boldsymbol{A}}_m(\omega(k))^{N_p-2}\right. \\ &\quad \left. + \cdots + \tilde{\boldsymbol{A}}_m(\omega(k)) + \boldsymbol{I}\right)\tilde{\boldsymbol{G}}. \end{aligned} \tag{32}$$

$$\begin{bmatrix} \left(\tilde{\boldsymbol{A}}_m(\omega(k)) + \tilde{\boldsymbol{B}}_m(\omega(k))\boldsymbol{K}_m\right)^{\mathrm{T}}\hat{\boldsymbol{P}}\left(\tilde{\boldsymbol{A}}_m(\omega(k)) + \tilde{\boldsymbol{B}}_m(\omega(k))\boldsymbol{K}_m\right) - \hat{\boldsymbol{P}} + \bar{\boldsymbol{Q}} + \boldsymbol{K}_m{}^{\mathrm{T}}\bar{\boldsymbol{R}}\boldsymbol{K}_m & * \\ \tilde{\boldsymbol{G}}^{\mathrm{T}}\hat{\boldsymbol{P}}\left(\tilde{\boldsymbol{A}}_m(\omega(k)) + \tilde{\boldsymbol{B}}_m(\omega(k))\boldsymbol{K}_m\right) & \tilde{\boldsymbol{G}}^{\mathrm{T}}\hat{\boldsymbol{P}}\tilde{\boldsymbol{G}} \end{bmatrix} < 0 \tag{23}$$

$$\begin{aligned} &\begin{bmatrix} \hat{\boldsymbol{P}} - \bar{\boldsymbol{Q}} - \boldsymbol{K}_m{}^{\mathrm{T}}\bar{\boldsymbol{R}}\boldsymbol{K}_m & 0 \\ 0 & 0 \end{bmatrix} \\ &- \begin{bmatrix} \left(\tilde{\boldsymbol{A}}_m(\omega(k)) + \tilde{\boldsymbol{B}}_m(\omega(k))\boldsymbol{K}_m\right)^{\mathrm{T}} \\ \tilde{\boldsymbol{G}}^{\mathrm{T}} \end{bmatrix}\hat{\boldsymbol{P}}\begin{bmatrix} \left(\tilde{\boldsymbol{A}}_m(\omega(k)) + \tilde{\boldsymbol{B}}_m(\omega(k))\boldsymbol{K}_m\right) & \tilde{\boldsymbol{G}}^{\mathrm{T}} \end{bmatrix} > 0 \end{aligned} \tag{24}$$

$$\begin{bmatrix} \hat{\boldsymbol{P}} - \bar{\boldsymbol{Q}} - \boldsymbol{K}_m{}^{\mathrm{T}}\bar{\boldsymbol{R}}\boldsymbol{K}_m & 0 & \left(\tilde{\boldsymbol{A}}_m(\omega(k)) + \tilde{\boldsymbol{B}}_m(\omega(k))\boldsymbol{K}_m\right)^{\mathrm{T}} \\ 0 & 0 & \tilde{\boldsymbol{G}}^{\mathrm{T}} \\ \left(\tilde{\boldsymbol{A}}_m(\omega(k)) + \tilde{\boldsymbol{B}}_m(\omega(k))\boldsymbol{K}_m\right) & \tilde{\boldsymbol{G}} & \hat{\boldsymbol{P}}^{-1} \end{bmatrix} > 0. \tag{25}$$

$$\begin{bmatrix} \hat{\boldsymbol{P}} - \bar{\boldsymbol{Q}} - \boldsymbol{K}_m{}^{\mathrm{T}}\bar{\boldsymbol{R}}\boldsymbol{K}_m & \left(\tilde{\boldsymbol{A}}_m(\omega(k)) + \tilde{\boldsymbol{B}}_m(\omega(k))\boldsymbol{K}_m\right)^{\mathrm{T}} & 0 \\ \left(\tilde{\boldsymbol{A}}_m(\omega(k)) + \tilde{\boldsymbol{B}}_m(\omega(k))\boldsymbol{K}_m\right) & \hat{\boldsymbol{P}}^{-1} & \tilde{\boldsymbol{G}} \\ 0 & \tilde{\boldsymbol{G}}^{\mathrm{T}} & 0 \end{bmatrix} > 0. \tag{26}$$

Authorized licensed use limited to: NANJING UNIVERSITY OF AERONAUTICS AND ASTRONAUTICS. Downloaded on April 15,2022 at 03:18:40 UTC from IEEE Xplore. Restrictions apply.

Combining (32), (17) can be transformed into

$$\begin{aligned}&(\boldsymbol{G}_e((\boldsymbol{\Lambda}_m(\omega(k))+\boldsymbol{Z}_m(\omega(k))\boldsymbol{Y}\boldsymbol{G}^{-1})\tilde{\boldsymbol{X}}(k)\\&\quad+\boldsymbol{L}_m(\omega(k))\boldsymbol{y}_r(k)))^{\mathrm{T}}\\&(\boldsymbol{G}_e((\boldsymbol{\Lambda}_m(\omega(k))+\boldsymbol{Z}_m(\omega(k))\boldsymbol{Y}\boldsymbol{G}^{-1})\tilde{\boldsymbol{X}}(k)\\&\quad+\boldsymbol{L}_m(\omega(k))\boldsymbol{y}_r(k)))\leqslant\ell\end{aligned}$$

then the aforementioned formula is rewritten into the LMI as

$$\begin{bmatrix}\ell & * \\ \boldsymbol{G}_e\left(\left(\boldsymbol{\Lambda}_m(\omega(k))+\boldsymbol{Z}_m(\omega(k))\boldsymbol{Y}\boldsymbol{G}^{-1}\right)\tilde{\boldsymbol{X}}(k)\right.\\ \left.+\boldsymbol{L}_m(\omega(k))\boldsymbol{y}_r(k)\right) & I\end{bmatrix}\geqslant 0.$$

Pre- and postmultiplying by $\mathrm{diag}(\boldsymbol{I},\boldsymbol{G})$ and $\mathrm{diag}(\boldsymbol{I},\boldsymbol{G}^{\mathrm{T}})$, respectively, gives

$$\begin{bmatrix}\ell & * \\ \boldsymbol{G}_e((\boldsymbol{\Lambda}_m(\omega(k))\boldsymbol{G}+\boldsymbol{Z}_m(\omega(k))\boldsymbol{Y})\tilde{\boldsymbol{X}}(k)\\ +\boldsymbol{G}\boldsymbol{L}_m(\omega(k))\boldsymbol{y}_r(k)) & \boldsymbol{G}\boldsymbol{G}^{\mathrm{T}}\end{bmatrix}\geqslant 0$$

using (12) to further transform the aforementioned equation into

$$\begin{bmatrix}\ell & * \\ \boldsymbol{G}_e\left(\left(\boldsymbol{\Lambda}_{mj}\boldsymbol{G}+\boldsymbol{Z}_{mj}\boldsymbol{Y}\right)\tilde{\boldsymbol{X}}(k)+\boldsymbol{G}\boldsymbol{L}_{mj}\boldsymbol{y}_r(k)\right) & \boldsymbol{G}\boldsymbol{G}^{\mathrm{T}}\end{bmatrix}\\ \geqslant 0,\ j=1,2,\ldots,L \tag{33}$$

$$\begin{aligned}\boldsymbol{\Lambda}_{mj}&=\sum_{j=1}^{L}\sigma_{mj}\tilde{\boldsymbol{A}}_{mj}^{N_p},\\ \boldsymbol{Z}_{mj}&=\sum_{j=1}^{L}\sigma_{mj}\left(\left(\tilde{\boldsymbol{A}}_{mj}^{N_p-1}+\tilde{\boldsymbol{A}}_{mj}^{N_p-2}+\cdots+\tilde{\boldsymbol{A}}_{mj}+\boldsymbol{I}\right)\tilde{\boldsymbol{B}}_{mj}\right)\\ \boldsymbol{L}_{mj}&=\sum_{j=1}^{L}\sigma_{mj}\left(\left(\tilde{\boldsymbol{A}}_{mj}^{N_p-1}+\tilde{\boldsymbol{A}}_{mj}^{N_p-2}+\cdots+\tilde{\boldsymbol{A}}_{mj}+\boldsymbol{I}\right)\tilde{\boldsymbol{G}}\right)\end{aligned}$$

thus, when the inequality (33) holds, it can ensure that the condition (17) is satisfied.

Derivation of upper bound of $J(k)$: Summing (19) from $i=1$ to $i=N_p-1$, based on (16), gives

$$\begin{aligned}J(k)\leqslant&V\left(\tilde{\boldsymbol{X}}\left(k+1|k\right)\right)+\|\boldsymbol{u}(k)\|_{\boldsymbol{R}}^2+E\left(\tilde{\boldsymbol{X}}\left(k+N_p|k\right)\right)\\&-V\left(\tilde{\boldsymbol{X}}\left(k+N_p|k\right)\right).\end{aligned}\tag{34}$$

Since $V(\tilde{\boldsymbol{X}}(k+N_p|k))\geqslant 0$, (34) can be further converted to

$$\begin{aligned}J(k)\leqslant&V\left(\tilde{\boldsymbol{X}}\left(k+1|k\right)\right)+\|\boldsymbol{u}(k)\|_{\boldsymbol{R}}^2+E\left(\tilde{\boldsymbol{X}}\left(k+N_p|k\right)\right).\end{aligned}\tag{35}$$

Let the upper bounds of $V(\tilde{\boldsymbol{X}}(k))$ and $\|\boldsymbol{u}(k)\|_{\boldsymbol{R}}^2$ be δ and χ_0, respectively, then

$$\|\boldsymbol{u}(k)\|_{\boldsymbol{R}}^2\leqslant\chi_0,V\left(\tilde{\boldsymbol{X}}(k)\right)\leqslant\delta\tag{36}$$

based on (20) and Lemma 1, we can conclude that $V(\tilde{\boldsymbol{X}}(k+1|k))<V(\tilde{\boldsymbol{X}}(k))$. Then, coupled with (17), the upper bound of $J(k)$ is

$$J(k)<\delta+\chi_0+\ell$$

therefore, optimization (16) can be converted to optimization $J=\delta+\chi_0+\ell$.

Moreover, based on the Schur complements and $\boldsymbol{P}_j=\delta\boldsymbol{Q}_j^{-1}$, the condition (36) can be rewritten as inequalities (37) and (38), respectively.

$$\begin{bmatrix}\chi_0 & * \\ \boldsymbol{u}(k) & \bar{\boldsymbol{R}}^{-1}\end{bmatrix}\geqslant 0\tag{37}$$

$$\begin{bmatrix}1 & * \\ \tilde{\boldsymbol{X}}(k) & \boldsymbol{Q}_j\end{bmatrix}\geqslant 0,\ j=1,2,\ldots,L.\tag{38}$$

$$\begin{bmatrix}\boldsymbol{G}^{\mathrm{T}}+\boldsymbol{G}-\boldsymbol{Q}_j & \boldsymbol{G}^{\mathrm{T}}\left[\tilde{\boldsymbol{A}}_{mj}+\tilde{\boldsymbol{B}}_{mj}\boldsymbol{K}_m\right]^{\mathrm{T}} & \boldsymbol{G}^{\mathrm{T}}\bar{\boldsymbol{Q}}^{1/2} & \boldsymbol{G}^{\mathrm{T}}{\boldsymbol{K}_m}^{\mathrm{T}}\bar{\boldsymbol{R}}^{1/2}\\ & \boldsymbol{Q}_j & \delta\tilde{\boldsymbol{G}} & 0\\ & * & \delta\boldsymbol{I} & 0\\ & * & * & \delta\boldsymbol{I}\end{bmatrix}>0,\ j=1,2,\ldots,L\tag{28}$$

$$\begin{aligned}&\min_{\boldsymbol{Y},\boldsymbol{Q}_j,\boldsymbol{U}}\ J=\delta+\chi_0+\ell\\&s.t.(20):=\begin{bmatrix}\boldsymbol{G}^{\mathrm{T}}+\boldsymbol{G}-\boldsymbol{Q}_j & * & * & *\\ \tilde{\boldsymbol{A}}_{mj}\boldsymbol{G}+\tilde{\boldsymbol{B}}_{mj}\boldsymbol{Y} & \boldsymbol{Q}_j & * & *\\ \bar{\boldsymbol{Q}}^{1/2}\boldsymbol{G} & \delta\tilde{\boldsymbol{G}}^{\mathrm{T}} & \delta\boldsymbol{I} & *\\ \bar{\boldsymbol{R}}^{1/2}\boldsymbol{Y} & 0 & 0 & \delta\boldsymbol{I}\end{bmatrix}>0,\ j=1,2,\ldots,L\\&\begin{bmatrix}\ell & * \\ \boldsymbol{G}_e\left(\left(\boldsymbol{\Lambda}_{mj}\boldsymbol{G}+\boldsymbol{Z}_{mj}\boldsymbol{Y}\right)\tilde{\boldsymbol{X}}(k)+\boldsymbol{G}\boldsymbol{L}_{mj}\boldsymbol{y}_r(k)\right) & \boldsymbol{G}\boldsymbol{G}^{\mathrm{T}}\end{bmatrix}\geqslant 0,\ j=1,2,\ldots,L\\&\begin{bmatrix}\chi_0 & * \\ \boldsymbol{u}(k) & \bar{\boldsymbol{R}}^{-1}\end{bmatrix}\geqslant 0\\&\begin{bmatrix}1 & * \\ \tilde{\boldsymbol{X}}(k) & \boldsymbol{Q}_j\end{bmatrix}\geqslant 0,\ j=1,2,\ldots,L\\&\begin{bmatrix}\boldsymbol{U} & \boldsymbol{Y} \\ * & \boldsymbol{G}^{\mathrm{T}}+\boldsymbol{G}-\boldsymbol{Q}_j\end{bmatrix}\geqslant 0,\boldsymbol{U}_{i_ui_u}\leqslant\boldsymbol{u}_{i_u,\max}^2,\ i_u=1,\ldots,n_u,\ j=1,2,\ldots,L\end{aligned}\tag{29}$$

Authorized licensed use limited to: NANJING UNIVERSITY OF AERONAUTICS AND ASTRONAUTICS. Downloaded on April 15,2022 at 03:18:40 UTC from IEEE Xplore. Restrictions apply.

Derivation of control constraints According to $V(\tilde{\boldsymbol{X}}(k)) \leqslant \delta$ and condition (20), we can know that

$$\begin{aligned}&\tilde{\boldsymbol{X}}(k+i|k)^{\mathrm{T}}\boldsymbol{P}_j\tilde{\boldsymbol{X}}(k+i|k)\\&\leqslant \tilde{\boldsymbol{X}}(k)^{\mathrm{T}}\boldsymbol{P}_j\tilde{\boldsymbol{X}}(k)\leqslant\delta\\&\Leftrightarrow \tilde{\boldsymbol{X}}(k+i|k)^{\mathrm{T}}{\boldsymbol{Q}_j}^{-1}\tilde{\boldsymbol{X}}(k+i|k)\\&\leqslant \tilde{\boldsymbol{X}}(k)^{\mathrm{T}}{\boldsymbol{Q}_j}^{-1}\tilde{\boldsymbol{X}}(k)\leqslant 1,\ i\geqslant 0.\end{aligned}$$

Define $\|\boldsymbol{u}(k+i)\|_{\max}\triangleq\max\|\boldsymbol{u}_{iu}(k+i)\|^2$, $i_u=1,2,\ldots,n_u$. Combining the aforementioned formula, (14), and $\boldsymbol{Y}=\boldsymbol{K}_m\boldsymbol{G}$, $\|\boldsymbol{u}(k+i)\|_{\max}$ can be rewritten as

$$\begin{aligned}\|\boldsymbol{u}(k+i)\|_{\max}&=\left\|\boldsymbol{K}_m\tilde{\boldsymbol{X}}(k+i|k)\right\|_{\max}\\&=\left\|\boldsymbol{Y}\boldsymbol{G}^{-1}\tilde{\boldsymbol{X}}(k+i|k)\right\|_{\max}\\&=\left\|\boldsymbol{Y}\boldsymbol{G}^{-1}\boldsymbol{Q}_j^{1/2}\boldsymbol{Q}_j^{-1/2}\tilde{\boldsymbol{X}}(k+i|k)\right\|_{\max}\\&\leqslant\left\|\boldsymbol{Y}\boldsymbol{G}^{-1}\boldsymbol{Q}_j^{1/2}\right\|_{\max}.\end{aligned}\tag{39}$$

Since $\boldsymbol{G}$ satisfies $0<\boldsymbol{G}^{\mathrm{T}}+\boldsymbol{G}-\boldsymbol{Q}_j\leqslant\boldsymbol{G}^{\mathrm{T}}{\boldsymbol{Q}_j}^{-1}\boldsymbol{G}$ [23], it can be obtained that

$$\left(\boldsymbol{G}^{-1}\right)\boldsymbol{Q}_j\left(\boldsymbol{G}^{-1}\right)^{\mathrm{T}}\leqslant\left(\boldsymbol{G}^{\mathrm{T}}+\boldsymbol{G}-\boldsymbol{Q}_j\right)^{-1}$$

based on the aforementioned equation, (39) can be further rewritten as

$$\begin{aligned}\|\boldsymbol{u}(k+i)\|_{\max}&\leqslant\left\|\boldsymbol{Y}\boldsymbol{G}^{-1}\boldsymbol{Q}_j^{1/2}\right\|_{\max}\\&\leqslant\left\|\boldsymbol{Y}\left(\boldsymbol{G}^{\mathrm{T}}+\boldsymbol{G}-\boldsymbol{Q}_j\right)^{-1/2}\right\|_{\max}\end{aligned}\tag{40}$$

thus, the control inputs of the subsystem (31) meet the following condition:

$$\boldsymbol{u}_{i_u,\max}^2-\left(\boldsymbol{Y}\left(\boldsymbol{G}^{\mathrm{T}}+\boldsymbol{G}-\boldsymbol{Q}_j\right)^{-1}\boldsymbol{Y}^{\mathrm{T}}\right)_{i_ui_u}\geqslant 0.$$

Set a real symmetric matrix $\boldsymbol{U}\in\mathbb{R}^{n_u\times n_u}$, the constraint can be transformed into

$$\begin{aligned}&\begin{bmatrix}\boldsymbol{U}&\boldsymbol{Y}\\*&\boldsymbol{G}^{\mathrm{T}}+\boldsymbol{G}-\boldsymbol{Q}_j\end{bmatrix}\geqslant 0\\&\boldsymbol{U}_{i_ui_u}\leqslant u_{i_u,\max}^2,\ i_u=1,\ldots,n_u,\ j=1,2,\ldots,L.\end{aligned}\tag{41}$$

In addition, to realize the stable switching between models, we introduce the GMs theory on the basis of Theorem 1 to obtain a closed-loop system that satisfies the specified stability requirements. First, the related definitions and lemmas of GMs are introduced.

LEMMA 2 [37] Let υ_Ω map $\mathbb{R}^{n\times n}$ into $\mathbb{C}$, if the following equation holds for $\boldsymbol{A}_c\in\bar{S}(\Omega)$:

$$\boldsymbol{A}_c\in\bar{S}(\Omega)\Leftrightarrow\upsilon_\Omega(\boldsymbol{A}_c)=0\tag{42}$$

it means that the map υ_Ω guards $S(\Omega)$.

In Lemma 2, $\boldsymbol{A}_c$ is the closed system matrix. Ω indicates an open subset in the complex plane, which is defined as follows:

$$\Omega=\left\{s\in\mathbb{C}:\boldsymbol{W}+s\boldsymbol{M}+\bar{s}\boldsymbol{M}^{\mathrm{T}}<0\right\}$$

where $\boldsymbol{W}$ and $\boldsymbol{M}=\boldsymbol{M}^{\mathrm{T}}$ are fixed real matrices, $\bar{s}$ is the conjugate transposition of s. $S(\Omega)=\{\boldsymbol{A}_c\in\mathbb{R}^{n\times n},\lambda(\boldsymbol{A}_c)\subset\Omega\}$,

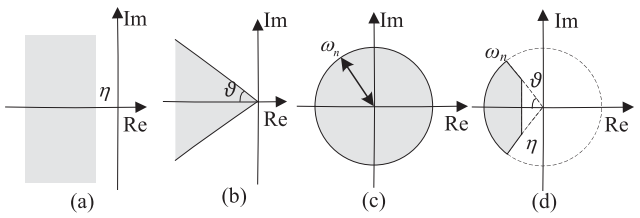

Fig. 3. Classic regions.

$\bar{S}(\Omega)$ denotes closure of the set $S(\Omega)$. Some classical regions of GMs (see Fig. 3) can be found in [37].

The next Lemma 3 describes the necessary and sufficient condition for the pole placement in a stability region Ω.

LEMMA 3 [38] A matrix $\boldsymbol{A}_c$ is stable relative to Ω, if and only if there exists a positive definite symmetric matrix P such that

$$\boldsymbol{W}\otimes\boldsymbol{P}+\boldsymbol{M}\otimes(\boldsymbol{A}_c\boldsymbol{P})+\boldsymbol{M}^{\mathrm{T}}\otimes(\boldsymbol{A}_c\boldsymbol{P})^{\mathrm{T}}<0.$$

Here, $\otimes$ denotes the Kronecker product. Xiao *et al.* [39] provide the following necessary and sufficient conditions of useful stability regions.

1) For a region with the stability margin greater than η [see Fig. 3(a)], then $\boldsymbol{W}=2\eta$, $\boldsymbol{M}=\boldsymbol{I}$, and the matrix $\boldsymbol{A}_c$ is stable if and only if
$$\boldsymbol{A}_c\boldsymbol{P}+\boldsymbol{P}{\boldsymbol{A}_c}^{\mathrm{T}}+2\eta<0.\tag{43}$$
2) Conic sector centered at the origin denotes the area where the damping ratio is larger than ζ [see Fig. 3(b)], and the LMI constraint is described as
$$\begin{bmatrix}\sin\vartheta\left(\boldsymbol{A}_c\boldsymbol{P}+\boldsymbol{P}\boldsymbol{A}_c^{\mathrm{T}}\right)&\cos\vartheta\left(\boldsymbol{A}_c\boldsymbol{P}-\boldsymbol{P}\boldsymbol{A}_c^{\mathrm{T}}\right)\\\cos\vartheta\left(\boldsymbol{P}\boldsymbol{A}_c^{\mathrm{T}}-\boldsymbol{A}_c\boldsymbol{P}\right)&\sin\vartheta\left(\boldsymbol{A}_c\boldsymbol{P}+\boldsymbol{P}\boldsymbol{A}_c^{\mathrm{T}}\right)\end{bmatrix}<0\tag{44}$$
where $\vartheta=\arccos(\zeta)$.
3) Let $\omega_n(\omega_n>0)$ be the radius of a circle shown in Fig. 3(c), and the LMI constraint is
$$\begin{bmatrix}-\omega_n\boldsymbol{P}&\boldsymbol{A}_c\boldsymbol{P}\\\boldsymbol{P}\boldsymbol{A}_c^{\mathrm{T}}&-\omega_n\boldsymbol{P}\end{bmatrix}<0.\tag{45}$$
4) If and only if constraints (43) and (45) are satisfied simultaneously, the stable region of the matrix $\boldsymbol{A}_c$ is shown in Fig. 3(d).

LEMMA 4 The control law $\boldsymbol{K}_m=\boldsymbol{Y}\boldsymbol{G}^{-1}$ makes the mth closed-loop subsystem (15) Ω-stable and minimizes the performance index function (16) if there exist $\boldsymbol{Q}_j(j=1,\ldots,L)$, $\boldsymbol{G}$, $\boldsymbol{Y}$ and scalars $\delta\geqslant 0$, $\chi_0\geqslant 0$, $\ell\geqslant 0$ can solve the following optimization problem (46)ndash;(52) shown at the bottom of next page.

PROOF Based on Theorem 1, (20), (33), (37), (38), and (41) define the necessary LMIs to find a feasible feedback control law so that the closed-loop subsystem is robustly asymptotically stable and the performance index (16) is minimized. Moreover, according to Lemma 3, it is known that the closed-loop subsystem (15) is Ω stable [stable

Authorized licensed use limited to: NANJING UNIVERSITY OF AERONAUTICS AND ASTRONAUTICS. Downloaded on April 15,2022 at 03:18:40 UTC from IEEE Xplore. Restrictions apply.

$$\min_{\boldsymbol{Y},\boldsymbol{Q}_j,\boldsymbol{U}} \delta + \chi_0 + \ell \quad s.t.(20),(33),(37),(38),(41),(47)-(49) \tag{46}$$

$$\left(\tilde{\boldsymbol{A}}_{mj}\boldsymbol{G}+\tilde{\boldsymbol{B}}_{mj}\boldsymbol{Y}\right)+\left(\tilde{\boldsymbol{A}}_{mj}\boldsymbol{G}+\tilde{\boldsymbol{B}}_{mj}\boldsymbol{Y}\right)^{\mathrm{T}}+2\eta<0,\ j=1,2,\ldots,L \tag{47}$$

$$\begin{bmatrix} \sin\vartheta\cdot\left[\left(\tilde{\boldsymbol{A}}_{mj}\boldsymbol{G}+\tilde{\boldsymbol{B}}_{mj}\boldsymbol{Y}\right)+\left(\tilde{\boldsymbol{A}}_{mj}\boldsymbol{G}+\tilde{\boldsymbol{B}}_{mj}\boldsymbol{Y}\right)^{\mathrm{T}}\right] & \cos\vartheta\cdot\left[\left(\tilde{\boldsymbol{A}}_{mj}\boldsymbol{G}+\tilde{\boldsymbol{B}}_{mj}\boldsymbol{Y}\right)-\left(\tilde{\boldsymbol{A}}_{mj}\boldsymbol{G}+\tilde{\boldsymbol{B}}_{mj}\boldsymbol{Y}\right)^{\mathrm{T}}\right] \\ & \sin\vartheta\cdot\left[\left(\tilde{\boldsymbol{A}}_{mj}\boldsymbol{G}+\tilde{\boldsymbol{B}}_{mj}\boldsymbol{Y}\right)+\left(\tilde{\boldsymbol{A}}_{mj}\boldsymbol{G}+\tilde{\boldsymbol{B}}_{mj}\boldsymbol{Y}\right)^{\mathrm{T}}\right] \end{bmatrix}<0 \tag{48}$$

$$j=1,2,\ldots,L$$

$$\begin{bmatrix} -\omega_n\left(\boldsymbol{G}^{\mathrm{T}}+\boldsymbol{G}\right) & \left(\tilde{\boldsymbol{A}}_{mj}\boldsymbol{G}+\tilde{\boldsymbol{B}}_{mj}\boldsymbol{Y}\right) \\ & -\omega_n\left(\boldsymbol{G}^{\mathrm{T}}+\boldsymbol{G}\right) \end{bmatrix}<0,\ j=1,2,\ldots,L. \tag{49}$$

$$\tilde{\boldsymbol{A}}_{mc}\left(\omega(k)\right)\hat{\boldsymbol{Q}}+\hat{\boldsymbol{Q}}\tilde{\boldsymbol{A}}_{mc}(\omega(k))^{\mathrm{T}}+2\eta<0 \tag{50}$$

$$\begin{bmatrix} \sin\vartheta\left(\tilde{\boldsymbol{A}}_{mc}\left(\omega(k)\right)\hat{\boldsymbol{Q}}+\hat{\boldsymbol{Q}}\tilde{\boldsymbol{A}}_{mc}(\omega(k))^{\mathrm{T}}\right) & \cos\vartheta\left(\tilde{\boldsymbol{A}}_{mc}\left(\omega(k)\right)\hat{\boldsymbol{Q}}-\hat{\boldsymbol{Q}}\tilde{\boldsymbol{A}}_{mc}(\omega(k))^{\mathrm{T}}\right) \\ \cos\vartheta\left(\hat{\boldsymbol{Q}}\tilde{\boldsymbol{A}}_{mc}(\omega(k))^{\mathrm{T}}-\tilde{\boldsymbol{A}}_{mc}\left(\omega(k)\right)\hat{\boldsymbol{Q}}\right) & \sin\vartheta\left(\tilde{\boldsymbol{A}}_{mc}\left(\omega(k)\right)\hat{\boldsymbol{Q}}+\hat{\boldsymbol{Q}}\tilde{\boldsymbol{A}}_{mc}(\omega(k))^{\mathrm{T}}\right) \end{bmatrix}<0 \tag{51}$$

$$\begin{bmatrix} -\omega_n\hat{\boldsymbol{Q}} & \tilde{\boldsymbol{A}}_{mc}\left(\omega(k)\right)\hat{\boldsymbol{Q}} \\ \hat{\boldsymbol{Q}}\tilde{\boldsymbol{A}}_{mc}(\omega(k))^{\mathrm{T}} & -\omega_n\hat{\boldsymbol{Q}} \end{bmatrix}<0 \tag{52}$$

region is Fig. 3(d)], if and only if the following inequalities hold: where $\tilde{\boldsymbol{A}}_{mc}(\omega(k))=\tilde{\boldsymbol{A}}_m(\omega(k))+\tilde{\boldsymbol{B}}_m(\omega(k))\boldsymbol{K}_m$, and $\hat{\boldsymbol{Q}}=\sum_{j=1}^{L}\sigma_{mj}\boldsymbol{Q}_j$.

As (50)–(52) contain uncertain term and control parameters, it is impossible to directly solve these LMIs. Therefore, it needs to be converted. First, based on (12), (50)–(52) are transformed into the polytopic form where $j=1,2,\ldots,L$. Because of $\sum_{j=1}^{L}\sigma_{mj}=1$, (53) can be further rewritten to

$$\left(\tilde{\boldsymbol{A}}_{mj}+\tilde{\boldsymbol{B}}_{mj}\boldsymbol{K}_m\right)\boldsymbol{Q}_j+\boldsymbol{Q}_j\left(\tilde{\boldsymbol{A}}_{mj}+\tilde{\boldsymbol{B}}_{mj}\boldsymbol{K}_m\right)^{\mathrm{T}}+2\eta<0 \tag{56}$$

then combined with $\boldsymbol{G}^{\mathrm{T}}+\boldsymbol{G}-\boldsymbol{Q}_j>0$ and $\boldsymbol{K}_m=\boldsymbol{Y}\boldsymbol{G}^{-1}$, (54)–(56) can be converted to where $G=(\boldsymbol{I}+\boldsymbol{G}^{-1}\boldsymbol{G}^{\mathrm{T}})$. Because $\boldsymbol{G}>0$, so $G>\boldsymbol{I}$, (57)–(59) are eventually simplified to the form shown in (47)–(49).

Thus, the inequalities (20), (33), (37), (38), (41), and (47)–(49) ensure that the closed-loop subsystem is Ω stable, and upper bounds on the control amplitude are satisfied. ■

Although the control performance can be improved by extending the predictive horizon when using the control law given via Lemma 4 for the trajectory tracking, it will cause a substantial increase in the number of optimization variables and matrix inequalities. According to [40], the computational complexity of solving each subsystem optimization problem (46) is proportional to ${m_{\mathrm{var}}}^3 n_{\mathrm{inequ}}$, where m_{var} is the number of optimization variables and n_{inequ} is the number of matrix inequalities. Therefore, compared with the general robust predictive controller, the computational burden of the control law $\boldsymbol{K}=\boldsymbol{Y}\boldsymbol{G}^{-1}$ obtained from (46) rises exponentially as the problem size increases.

$$\sum_{j=1}^{L}\sigma_{mj}\left(\left(\tilde{\boldsymbol{A}}_{mj}+\tilde{\boldsymbol{B}}_{mj}\boldsymbol{K}_m\right)\boldsymbol{Q}_j+\boldsymbol{Q}_j\left(\tilde{\boldsymbol{A}}_{mj}+\tilde{\boldsymbol{B}}_{mj}\boldsymbol{K}_m\right)^{\mathrm{T}}\right)+2\eta<0 \tag{53}$$

$$\begin{bmatrix} \sin\vartheta\cdot\left[\left(\tilde{\boldsymbol{A}}_{mj}+\tilde{\boldsymbol{B}}_{mj}\boldsymbol{K}_m\right)\boldsymbol{Q}_j+\boldsymbol{Q}_j\left(\tilde{\boldsymbol{A}}_{mj}+\tilde{\boldsymbol{B}}_{mj}\boldsymbol{K}_m\right)^{\mathrm{T}}\right] & \cos\vartheta\cdot\left[\left(\tilde{\boldsymbol{A}}_{mj}+\tilde{\boldsymbol{B}}_{mj}\boldsymbol{K}_m\right)\boldsymbol{Q}_j-\boldsymbol{Q}_j\left(\tilde{\boldsymbol{A}}_{mj}+\tilde{\boldsymbol{B}}_{mj}\boldsymbol{K}_m\right)^{\mathrm{T}}\right] \\ & \sin\vartheta\cdot\left[\left(\tilde{\boldsymbol{A}}_{mj}+\tilde{\boldsymbol{B}}_{mj}\boldsymbol{K}_m\right)\boldsymbol{Q}_j+\boldsymbol{Q}_j\left(\tilde{\boldsymbol{A}}_{mj}+\tilde{\boldsymbol{B}}_{mj}\boldsymbol{K}_m\right)^{\mathrm{T}}\right] \end{bmatrix}<0 \tag{54}$$

$$\begin{bmatrix} -\omega_n\boldsymbol{Q}_j & \left(\tilde{\boldsymbol{A}}_{mj}+\tilde{\boldsymbol{B}}_{mj}\boldsymbol{K}_m\right)\boldsymbol{Q}_j \\ & -\omega_n\boldsymbol{Q}_j \end{bmatrix}<0 \tag{55}$$

$$\left(\tilde{\boldsymbol{A}}_{mj}\boldsymbol{G}+\tilde{\boldsymbol{B}}_{mj}\boldsymbol{Y}\right)G+G^{\mathrm{T}}\left(\tilde{\boldsymbol{A}}_{mj}\boldsymbol{G}+\tilde{\boldsymbol{B}}_{mj}\boldsymbol{Y}\right)^{\mathrm{T}}+2\eta<0 \tag{57}$$

$$\begin{bmatrix} \sin\vartheta\cdot\left[\left(\tilde{\boldsymbol{A}}_{mj}\boldsymbol{G}+\tilde{\boldsymbol{B}}_{mj}\boldsymbol{Y}\right)G+G^{\mathrm{T}}\left(\tilde{\boldsymbol{A}}_{mj}\boldsymbol{G}+\tilde{\boldsymbol{B}}_{mj}\boldsymbol{Y}\right)^{\mathrm{T}}\right] & \cos\vartheta\cdot\left[\left(\tilde{\boldsymbol{A}}_{mj}\boldsymbol{G}+\tilde{\boldsymbol{B}}_{mj}\boldsymbol{Y}\right)G-G^{\mathrm{T}}\left(\tilde{\boldsymbol{A}}_{mj}\boldsymbol{G}+\tilde{\boldsymbol{B}}_{mj}\boldsymbol{Y}\right)^{\mathrm{T}}\right] \\ & \sin\vartheta\cdot\left[\left(\tilde{\boldsymbol{A}}_{mj}\boldsymbol{G}+\tilde{\boldsymbol{B}}_{mj}\boldsymbol{Y}\right)G+G^{\mathrm{T}}\left(\tilde{\boldsymbol{A}}_{mj}\boldsymbol{G}+\tilde{\boldsymbol{B}}_{mj}\boldsymbol{Y}\right)^{\mathrm{T}}\right] \end{bmatrix}<0 \tag{58}$$

$$\begin{bmatrix} -\omega_n\left(\boldsymbol{G}^{\mathrm{T}}+\boldsymbol{G}\right) & \left(\tilde{\boldsymbol{A}}_{mj}\boldsymbol{G}+\tilde{\boldsymbol{B}}_{mj}\boldsymbol{Y}\right)G \\ & -\omega_n\left(\boldsymbol{G}^{\mathrm{T}}+\boldsymbol{G}\right) \end{bmatrix}<0 \tag{59}$$

Authorized licensed use limited to: NANJING UNIVERSITY OF AERONAUTICS AND ASTRONAUTICS. Downloaded on April 15,2022 at 03:18:40 UTC from IEEE Xplore. Restrictions apply.

To meet the requirement of real-time control, a robust comprehensive design method is proposed to improve the solution process of the aforementioned control law. By observing Lemma 4, we can find that (20), (41), and (47)–(49) are all independent of state variables. Therefore, δ, $\boldsymbol{G}$, $\boldsymbol{Y}$, and $\boldsymbol{Q}_j$ in (20), (41), and (47)–(49) can be calculated offline, then, under the constraints (33), (37), and (38), the χ_0, ℓ, and $\boldsymbol{u}(k)$ are optimized online.

LEMMA 5 For the mth uncertain subsystem (15), assumed that there are two sets of sequences $\{\delta_1, \tilde{\boldsymbol{F}}^1_1, \ldots, \tilde{\boldsymbol{F}}^1_{N_p-1}\}$ and $\{\delta_2, \tilde{\boldsymbol{F}}^2_1, \ldots, \tilde{\boldsymbol{F}}^2_{N_p-1}\}$ satisfying the conditions (20), (41), and (47)–(49). Then, its combination $\{\hbar_1\delta_1 + \hbar_2\delta_2, \hbar_1\tilde{\boldsymbol{F}}^1_1 + \hbar_2\tilde{\boldsymbol{F}}^2_1, \ldots, \hbar_1\tilde{\boldsymbol{F}}^1_{N_p-1} + \hbar_2\tilde{\boldsymbol{F}}^2_{N_p-1}\}$ also meets the conditions (20), (41), and (47)–(49), where $\tilde{\boldsymbol{F}}_i = \{\boldsymbol{G}_i, \boldsymbol{Q}_{i,j}, \boldsymbol{Y}_i\}$, $i = 1, 2, \ldots, N_p - 1$, $\hbar_1 + \hbar_2 \leqslant 1$, $\hbar_d \geqslant 0 (d = 1, 2)$.

PROOF: The coefficients $\hbar_1$ and $\hbar_2$ are multiplied by the corresponding inequalities (20), (41), and (47)–(49) of $\tilde{\boldsymbol{F}}^1_i$ and $\tilde{\boldsymbol{F}}^2_i$, respectively, and then, the aforementioned conclusions can be obtained by adding them. ■

It can be seen from Lemma 5 that when the corresponding performance indexes of two sequences $\{\delta_1, \tilde{\boldsymbol{F}}^1_1, \ldots, \tilde{\boldsymbol{F}}^1_{N_p-1}\}$ and $\{\delta_2, \tilde{\boldsymbol{F}}^2_1, \ldots, \tilde{\boldsymbol{F}}^2_{N_p-1}\}$ are different in the offline design; then, under the constraints (33), (37), and (38), the performance index $J = \chi_0 + \ell + (\hbar_1 + \cdots + \hbar_{N_p-1})\delta_1 + (\hbar_{N_p} + \cdots + \hbar_{2(N_p-1)})\delta_2$ can be optimized via online optimizing the $\hbar_i$ $(i = 1, 2, \ldots, N_p - 1)$, χ_0, and ℓ, also the subsystem control input can be obtained. The design steps of the robust comprehensive design method are described as follows.

According to the aforementioned process, it can be seen that this method can improve the online computing rate by reducing the number of LMIs calculated online.

2) *Switching Rule Based on GM:* The local controller obtained via the robust comprehensive design method can guarantee system stability in the subregion. However, for the control system based on multimodel, improper controller switching may lead to system instability between stable controllers. Therefore, a switching rule based on the GM is presented to realize automatic switching and keep the system stability. In order to analyze the largest variation range of parameter that guarantees the stability of parametric matrix, the following lemma is introduced.

LEMMA 6 [39] Let $\boldsymbol{A}_c(r)$ be a matrix in the uncertain parameter r; if $\boldsymbol{A}_c(r_0)$ is stable with respect to Ω, that is, $\boldsymbol{A}_c(r_0) \in S(\Omega)$. Assuming that r^- is regarded as the largest root of $\upsilon_\Omega[\boldsymbol{A}_c(r)] = 0$ within the interval $(-\infty, r_0)$ (or $r^- = -\infty$ if none exist). Similarly, r^+ is considered as the smallest root of $\upsilon_\Omega[\boldsymbol{A}_c(r)] = 0$ within the internal $(r_0, +\infty)$ (or $r^+ = +\infty$ if none exist). In that way, $\boldsymbol{A}_c(r)$ is stable relative to Ω for all $r \in (r^-, r^+)$. In addition, the interval (r^-, r^+) is the largest one containing r_0.

Suppose that under the working point k, the control parameter of the mth subsystem satisfies the stability domain Ω [Fig. 3(d)] obtained by Lemma 4 is $\boldsymbol{K}_m$. Based on Lemma 6, the switching rule based on GM (the schematic diagram is shown in Fig. 4) is stated as follows:

1) The piecewise linear system (9) is used for numerical fitting in advance to generate the LPV model with parameters δV and δh:

$$\begin{cases} \boldsymbol{X}(k+1) = \boldsymbol{A}(\delta V, \delta h)\boldsymbol{X}(k) + \boldsymbol{B}(\delta V, \delta h)\boldsymbol{u}(k) \\ \boldsymbol{y}(k) = \boldsymbol{C}(\delta V, \delta h)\boldsymbol{X}(k) \end{cases}$$

Algorithm 2: The Robust Comprehensive Design Method.

Offline:

Step 1 Set the appropriate δ_1 and δ_2, and $(\delta_2 \ll \delta_1)$. The attractive region of polytopic model is chosen as the optimization objective.

Step 2 Under inequality constraints (20), (41) and (47)-(49), find $\{\delta_1, \tilde{\boldsymbol{F}}^1_1, \ldots, \tilde{\boldsymbol{F}}^1_{N_p-1}\}$ and $\{\delta_2, \tilde{\boldsymbol{F}}^2_1, \ldots, \tilde{\boldsymbol{F}}^2_{N_p-1}\}$ to solve the following optimization problem

$$\min_{\tilde{\boldsymbol{F}}^1_i, \tilde{\boldsymbol{F}}^2_i} J = -\ln\left(\det\left(\boldsymbol{G}^1_i\right)\right), i = 1, 2, \ldots, N_p - 1$$
$$s.t.\ (20)\,(41)(47) - (49)$$

then the sequence $\{\delta_1, \tilde{\boldsymbol{F}}^1_1, \ldots, \tilde{\boldsymbol{F}}^1_{N_p-1}\}$ and $\{\delta_2, \tilde{\boldsymbol{F}}^2_1, \ldots, \tilde{\boldsymbol{F}}^2_{N_p-1}\}$ are obtained. The $\ln(\det(\boldsymbol{G}))$ is proportional to the area covered of the elliptic set $O_s = \{\tilde{\boldsymbol{X}} | \tilde{\boldsymbol{X}}^{\mathrm{T}}\boldsymbol{G}^{-1}\tilde{\boldsymbol{X}} \leqslant 1\}$ [41], $\det(\cdot)$ represents the matrix determinant function.

Online:

Step 1 Determine system status and the sub-region of ASV at time k.

Step 2 Based on $\{\delta_1, \tilde{\boldsymbol{F}}^1_1, \ldots, \tilde{\boldsymbol{F}}^1_{N_p-1}\}$ and $\{\delta_2, \tilde{\boldsymbol{F}}^2_1, \ldots, \tilde{\boldsymbol{F}}^2_{N_p-1}\}$ obtained offline, the optimization problem of solving the control law based on Lemma 4 in the online process can be simplified to equation (60). Therefore, under constraints (33), (37), and (38), the problem (60) is optimized online to obtain the control input $\boldsymbol{u}(k)$.

$$\begin{aligned} &\min_{\boldsymbol{u}(k), \hbar_1, \ldots, \hbar_{N_p-1}, \ldots, \hbar_{2(N_p-1)}} J = \chi_0 + \ell \\ &\quad + \left(\hbar_1 + \cdots + \hbar_{N_p-1}\right)\delta_1 \\ &\quad + \left(\hbar_{N_p} + \cdots + \hbar_{2(N_p-1)}\right)\delta_2 \\ &s.t.\ \text{with} \boldsymbol{Q}_{m,j} = \tilde{\boldsymbol{Q}}_{m,j},\ \boldsymbol{G}_m = \tilde{\boldsymbol{G}}_m,\ \boldsymbol{Y}_m = \tilde{\boldsymbol{Y}}_m \\ &\quad \sum_{i=1}^{2(N_p-1)} \hbar_i \leqslant 1, \quad \hbar_i \geqslant 0 \\ &\quad \left(i = 1, \ldots, 2\left(N_p - 1\right);\ j = 1, 2, \ldots, L\right) \\ &\tilde{\boldsymbol{Q}}_{m,j} = \hbar_1\boldsymbol{Q}^1_{1,j} + \cdots + \hbar_{N_p-1}\boldsymbol{Q}^1_{N_p-1,j} + \hbar_{N_p}\boldsymbol{Q}^2_{1,j} + \cdots \\ &\quad + \hbar_{2(N_p-1)}\boldsymbol{Q}^2_{N_p-1,j} \end{aligned} \tag{60}$$

$$\begin{aligned} \tilde{\boldsymbol{G}}_m &= \hbar_1\boldsymbol{G}^1_1 + \cdots + \hbar_{N_p-1}\boldsymbol{G}^1_{N_p-1} + \hbar_{N_p}\boldsymbol{G}^2_1 + \cdots \\ &\quad + \hbar_{2(N_p-1)}\boldsymbol{G}^2_{N_p-1} \\ \tilde{\boldsymbol{Y}}_m &= \hbar_1\boldsymbol{Y}^1_1 + \cdots + \hbar_{N_p-1}\boldsymbol{Y}^1_{N_p-1} + \hbar_{N_p}\boldsymbol{Y}^2_1 + \cdots \\ &\quad + \hbar_{2(N_p-1)}\boldsymbol{Y}^2_{N_p-1} \end{aligned}$$

Authorized licensed use limited to: NANJING UNIVERSITY OF AERONAUTICS AND ASTRONAUTICS. Downloaded on April 15,2022 at 03:18:40 UTC from IEEE Xplore. Restrictions apply.

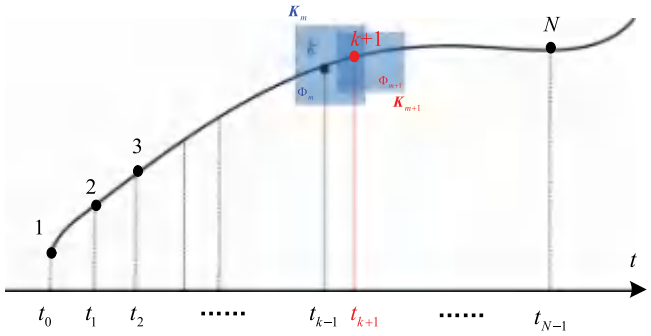

Fig. 4. Schematic diagram of improved switching rule.

where δV and δh are the symbols of speed and height, respectively. Then, the closed-loop state matrix under the control parameter $\boldsymbol{K}_m$ is $\tilde{\boldsymbol{A}}_c(\delta V, \delta h) = \tilde{\boldsymbol{A}}(\delta V, \delta h) + \tilde{\boldsymbol{B}}(\delta V, \delta h)\boldsymbol{K}_m$.

2) Let the target stability region be Ω_{obj}, which depends on the designer. Then, Lemma 6 is used to solve $\upsilon_{\Omega_{\text{obj}}}[\tilde{\boldsymbol{A}}_c(\delta V, \delta h)] = 0$ to obtain the maximum controllable interval $({V_m}^-, {V_m}^+) \times ({h_m}^-, {h_m}^+)$ that contains the current flight state, denoted as Φ_m. It is the maximum interval that the closed-loop system satisfies the stability region Ω_{obj} under the control parameter $\boldsymbol{K}_m$.

3) If the flight state of the ASV exceeds $3/4\Phi_m$, namely $V \geqslant 3/4(V_m^+ - V_m^-) + V_m^-$ or $h \geqslant 3/4(h_m^+ - h_m^-) + h_m^-$, the controller is adaptively switched, that is, the system state at this time is sampled, and the control law is updated to $\boldsymbol{K}_{m+1}$.

According to Fig. 4 and the aforementioned description of the switching rule, it can be known that based on this switching rule, the control law can be adaptively updated to realize the controller switching, and it ensures that controllable intervals under the adjacent control laws, such as Φ_m and Φ_{m+1}, have a certain degree of overlap ($\Phi_m \cap \Phi_{m+1} \neq 0$). In addition, Lemmas 4 and 6 show that the control law obtained under the constraint of GMs has the same stable region Ω_{obj} in its controllable interval. That is to say, this switching rule can ensure that the switching process has the following characteristics:

1) the next state model is still within the controllable interval of the current control law;
2) the controllable intervals of adjacent control laws have a certain overlap, and the stability regions of two control laws are consistent in the overlapping area.

3) *Stability Analysis:* THEOREM 2: Consider the uncertain system (11), if the local controllers satisfy conditions (20), (33), (37), (38), (41), and (47)–(49), and the switching between controllers is realized by the switching rule based on GM. Then, the closed-loop system is robustly Ω-stable.

PROOF Suppose, at sampling time k, the system state enters the subregion belonging to the mth controller designed for the linear model Γ_m. According to Theorem 1 and Lemma 4, the optimal solution $\{\delta_m^*(k), \boldsymbol{G}_m^*(k), \boldsymbol{Y}_m^*(k), \boldsymbol{Q}_{m,j}^*(k)\}$ of the mth subsystem is given, $\boldsymbol{K}_m^*(k) = \boldsymbol{Y}_m^*(k)\boldsymbol{G}_m^*(k)^{-1}$. The corresponding Lyapunov function is $V(\tilde{\boldsymbol{X}}_m(k))$

$$V(\tilde{\boldsymbol{X}}_m(k)) = \tilde{\boldsymbol{X}}_m(k)^{\mathrm{T}}\hat{\boldsymbol{P}}_m^*(k)\tilde{\boldsymbol{X}}_m(k)$$

where $\hat{\boldsymbol{P}}_m^*(k) = \sum_{j=1}^{L}\sigma_{mj}\boldsymbol{P}_{m,j}^*(k)$ and $\boldsymbol{P}_{m,j}^*(k) = \delta_m^*(k)\boldsymbol{Q}_{m,j}^*(k)^{-1}$.

According to Lemma 1, the constraint (20) is equivalent to

$$\begin{aligned}\tilde{\boldsymbol{X}}_m(k+1|k)^{\mathrm{T}}\hat{\boldsymbol{P}}_m^*(k)\tilde{\boldsymbol{X}}_{\underline{m}}(k+1|k) - \tilde{\boldsymbol{X}}_m(k)^{\mathrm{T}}\hat{\boldsymbol{P}}_m^*(k)\tilde{\boldsymbol{X}}_m(k)\\ < -\tilde{\boldsymbol{X}}_m(k)^{\mathrm{T}}\left[\bar{\boldsymbol{Q}} + \boldsymbol{K}_m^*(k)^{\mathrm{T}}\bar{\boldsymbol{R}}\boldsymbol{K}_m^*(k)\right]\tilde{\boldsymbol{X}}_m(k)\end{aligned} \tag{61}$$

then the following equation can be obtained from (61):

$$\tilde{\boldsymbol{X}}_m(k+1|k)^{\mathrm{T}}\hat{\boldsymbol{P}}_m^*(k)\tilde{\boldsymbol{X}}_m(k+1|k) < \tilde{\boldsymbol{X}}_m(k)^{\mathrm{T}}\hat{\boldsymbol{P}}_m^*(k)\tilde{\boldsymbol{X}}_m(k). \tag{62}$$

The constraint (38) is equivalent to $\tilde{\boldsymbol{X}}_m(k)^{\mathrm{T}}\hat{\boldsymbol{P}}_m^*(k)\tilde{\boldsymbol{X}}_m(k) \leqslant \delta$. It can be concluded from (62) that (38) is automatically satisfied if the initial state is feasible, so the $\{\delta_m^*(k), \boldsymbol{G}_m^*(k), \boldsymbol{Y}_m^*(k), \boldsymbol{Q}_{m,j}^*(k)\}$ is also the feasible solution of optimization problem (29) at time $k+1$. Assuming that the optimal solution at time $k+1$ is $\{\delta_m^*(k+1), \boldsymbol{G}_m^*(k+1), \boldsymbol{Y}_m^*(k+1), \boldsymbol{Q}_{m,j}^*(k+1)\}$ and $\boldsymbol{P}_{m,j}^*(k+1) = \delta_m^*(k+1)\boldsymbol{Q}_{m,j}^*(k+1)^{-1}$, then

$$\begin{aligned}&\tilde{\boldsymbol{X}}_m(k+1|k)^{\mathrm{T}}\hat{\boldsymbol{P}}_m^*(k+1)\tilde{\boldsymbol{X}}_m(k+1|k)\\ &< \tilde{\boldsymbol{X}}_m(k+1|k)^{\mathrm{T}}\hat{\boldsymbol{P}}_m^*(k)\tilde{\boldsymbol{X}}_m(k+1|k)\end{aligned} \tag{63}$$

combining (62) and (63), it is obvious that

$$V\left(\tilde{\boldsymbol{X}}_m(k+1)\right) < V\left(\tilde{\boldsymbol{X}}_m(k)\right). \tag{64}$$

Moreover, integrating (53)–(59), the constraints (47)–(49) are equivalent to unnumbered equation shown at the bottom of this page. where $\tilde{\boldsymbol{A}}_{mc}(\omega(k)) = \tilde{\boldsymbol{A}}_m(\omega(k)) + \tilde{\boldsymbol{B}}_m(\omega(k))\boldsymbol{K}_m^*$. According to Lemma 3, the aforementioned

$$\tilde{\boldsymbol{A}}_{mc}(\omega(k))\hat{\boldsymbol{Q}}_m^*(k) + \hat{\boldsymbol{Q}}_m^*(k)\tilde{\boldsymbol{A}}_{mc}(\omega(k))^{\mathrm{T}} + 2\eta < 0$$

$$\begin{bmatrix}\sin\vartheta\left(\tilde{\boldsymbol{A}}_{mc}(\omega(k))\hat{\boldsymbol{Q}}_m^*(k) + \hat{\boldsymbol{Q}}_m^*(k)\tilde{\boldsymbol{A}}_{mc}(\omega(k))^{\mathrm{T}}\right) & \cos\vartheta\left(\tilde{\boldsymbol{A}}_{mc}(\omega(k))\hat{\boldsymbol{Q}}_m^*(k) - \hat{\boldsymbol{Q}}_m^*(k)\tilde{\boldsymbol{A}}_{mc}(\omega(k))^{\mathrm{T}}\right)\\ \cos\vartheta\left(\hat{\boldsymbol{Q}}_m^*(k)\tilde{\boldsymbol{A}}_{mc}(\omega(k))^{\mathrm{T}} - \tilde{\boldsymbol{A}}_{mc}(\omega(k))\hat{\boldsymbol{Q}}_m^*(k)\right) & \sin\vartheta\left(\tilde{\boldsymbol{A}}_{mc}(\omega(k))\hat{\boldsymbol{Q}}_m^*(k) + \hat{\boldsymbol{Q}}_m^*(k)\tilde{\boldsymbol{A}}_{mc}(\omega(k))^{\mathrm{T}}\right)\end{bmatrix} < 0$$

$$\begin{bmatrix}-\omega_n\hat{\boldsymbol{Q}}_m^*(k) & \tilde{\boldsymbol{A}}_{mc}(\omega(k))\hat{\boldsymbol{Q}}_m^*(k)\\ \hat{\boldsymbol{Q}}_m^*(k)\tilde{\boldsymbol{A}}_{mc}(\omega(k))^{\mathrm{T}} & -\omega_n\hat{\boldsymbol{Q}}_m^*(k)\end{bmatrix} < 0$$

Authorized licensed use limited to: NANJING UNIVERSITY OF AERONAUTICS AND ASTRONAUTICS. Downloaded on April 15,2022 at 03:18:40 UTC from IEEE Xplore. Restrictions apply.

inequalities make sure that the current linear model Γ_m is Ω-stable under the control law $\boldsymbol{K}_m^*(k)$.

Thus, the mth local controller can guarantee the stability of the mth closed-loop subsystem, and the stable region is Ω [see Fig. 3(d)].

Consider the switching process between the mth controller (controller #m) and the #$m+1$th controller designed for the linear model Γ_{m+1}. According to the improved switching rule and Fig. 4, the switching point is located in the controllable overlapping area of #m and #$m+1$ controllers. Based on Lemmas 4 and 6, it can be seen that under constraints (47)–(49), the stability regions of #m and #$m+1$ controllers in the overlapping region are consistent. Therefore, the switching process is always within the stable range of the controller to ensure stable switching. The process will continue until $t_k = t_f$, then the last controller guarantee to converge to the desired state. ■

B. Real-Time Modification of Tracking Command

If the actual trajectory (x, h) is far from the reference trajectory (x_r, h_r), the controller would provide a high gain to quickly eliminate errors. Moreover, because of the high velocity and strict actuator constraints of ASVs, it is easy to cause actuator saturation. In addition, in the process of trajectory tracking, the aerospace vehicle is allowed to deviate the reference trajectory as long as it reaches the preset target position within the allowable time. Therefore, a transition trajectory can be designed between the reference trajectory and the actual trajectory [42], and then, the ASV tracks the transition reference trajectory to decompose the excessive initial deviation. In this way, the controller does not need to provide too high control energy to avoid saturation, which further improves the tracking accuracy.

The transient reference trajectory is designed as

$$\begin{cases} \dot{x}_d = V_d \cos\gamma_d \\ \dot{h}_d = V_d \sin\gamma_d. \end{cases} \tag{65}$$

Consider the error between the transient trajectory and reference trajectory satisfies the following equation:

$$\begin{cases} \dot{x}_r - \dot{x}_d = -k_1 (x_r - x_d) \\ \dot{h}_r - \dot{h}_d = -k_2 (h_r - h_d) \end{cases} \tag{66}$$

where k_1 and k_2 are positive scalars and given by the designer. According to the given reference trajectory $(x_r, h_r, V_r, \gamma_r)$ and (66), the transient reference trajectory $(x_d, h_d, V_d, \gamma_d)$ can be obtained by setting appropriate gains k_1 and k_2 to track the reference trajectory displacement (x_r, h_r) within a specified time.

Combining (1), (65), and (66), the speed V_d and flight-path angle γ_d of the transient trajectory can be calculated as follows:

$$\begin{cases} V_d = \sqrt{\begin{matrix}\left(V_r \cos\gamma_r + k_1 (x_r - x_d)\right)^2 + \\ \left(h_r \sin\gamma_r + k_2 (h_r - h_d)\right)^2\end{matrix}} \\ \gamma_d = \arctan\left(\frac{h_r \sin\gamma_r + k_2 (h_r - h_d)}{V_r \cos\gamma_r + k_1 (x_r - x_d)}\right). \end{cases} \tag{67}$$

Then, the ASV is transformed from tracking $\boldsymbol{y}_r = [x_r, h_r, V_r, \gamma_r, \alpha_r, q_r]^{\mathrm{T}}$ to track the modified trajectory $\boldsymbol{y}_d = [x_d, h_d, V_d, \gamma_d, \alpha_r, q_r]^{\mathrm{T}}$.

C. TRT Law

Here, the controller design based on Theorem 2 will be performed. For the uncertain system (11), a composite control law is proposed

$$\boldsymbol{u} = \boldsymbol{u}_m + \boldsymbol{K}_m(t)\tilde{\boldsymbol{X}}_d(t) \tag{68}$$

where $\boldsymbol{u}_m(t) = \sum_{m=1}^{n_k} \kappa_m \boldsymbol{u}_{\mathrm{eq,m}}$ is the control input at the equilibrium point, and $\boldsymbol{K}_m(t) = \sum_{m=1}^{n_k} \kappa_m \boldsymbol{K}_m(k)$ is the feedback control gain obtained by the RMMPC strategy. The subscript m represents the number of the subenvelope corresponding to the kth operating point, the expression of κ_m is

$$\kappa_m(t) = \begin{cases} 1 & [V(t), h(t)] \in \phi_m \\ 0 & \text{otherwise.} \end{cases}$$

Moreover, the form of $\tilde{\boldsymbol{X}}_d(t)$ is as follows:

$$\tilde{\boldsymbol{X}}_d(t) = \begin{bmatrix} \boldsymbol{X}(t) \\ \boldsymbol{C}\boldsymbol{X}(t) - \boldsymbol{y}_d(t) \end{bmatrix}$$

where $\boldsymbol{y}_d$ is the actual tracking signal, which can track the reference signal asymptotically.

V. SIMULATION STUDY

In this section, the robustness and tracking performance of the RMMPC law, the ability of the TRT scheme to quickly track and handle the initial errors is verified, respectively.

A. Simulation Conditions

The main characteristics of GHAME [26] and other relevant parameters for simulation are listed in Table I. The aerodynamic and propulsion data in [26] and [27] are used as nominal values for the controller design. In the simulation, 30% uncertainty of lift, drag, and moment is considered, namely

$$\begin{aligned} L_{\text{vehicle}} = (1 + 0.3\omega)\, L_0,\, D_{\text{vehicle}} = (1 + 0.3\omega)\, D_0,\, M_y \\ = (1 + 0.3\omega)\, M_{y0} \end{aligned} \tag{69}$$

where, L_0, D_0, and M_{y0} are the nominal lift, drag, and pitch moment, $\omega \in [-1, 1]$ indicates the random variable.

Remark: The parameters related to the controller design in Table I, such as $\boldsymbol{Q}_e$, are selected through the "trial and error" process, which are suitable for the simulation object in this article.

The reference trajectory $\boldsymbol{y}_r$ is obtained by the pseudospectral method. Here, the tracking range is $\{(x, h)|(x_0, h_0) = (0\text{km}, 9.6\text{km}) \sim (x_f, h_f) = (11.7\text{km}, 10.05\text{km})\}$, and the time is [0, 20s]. In addition, to ensure the normal operation of engine, the amplitude of AOA does not exceed 8°. The control constraints are as follows:

$$\begin{cases} |\delta_e| \leqslant 20^{\circ} & 0\tilde{\text{s}} \leqslant t \leqslant 20\text{s} \\ 0.2 < \phi \leqslant 1.4 & 0\tilde{\text{s}} \leqslant t \leqslant 20\text{s}. \end{cases} \tag{70}$$

Authorized licensed use limited to: NANJING UNIVERSITY OF AERONAUTICS AND ASTRONAUTICS. Downloaded on April 15,2022 at 03:18:40 UTC from IEEE Xplore. Restrictions apply.

TABLE I
List of Parameters

Parameter	Value
c	22.86 m
S_{ref}	557.42 m^2
$m_{\_\text{vehicle}}$	26617 kg
inertia moment (full load) I_{y1}	$31.59 \times 10^6 \text{kg} \cdot \text{m}^2$
inertia moment (fuel turn-out) I_{y2}	$19.25 \times 10^6 \text{kg} \cdot \text{m}^2$
N_p	4
sampling time	0.1 s
bound of AOA	8^{o}
$\boldsymbol{Q}_e$	diag [50, 50, 15, 3, 15, 3]
$\boldsymbol{R}$	diag [0.1, 0.1]

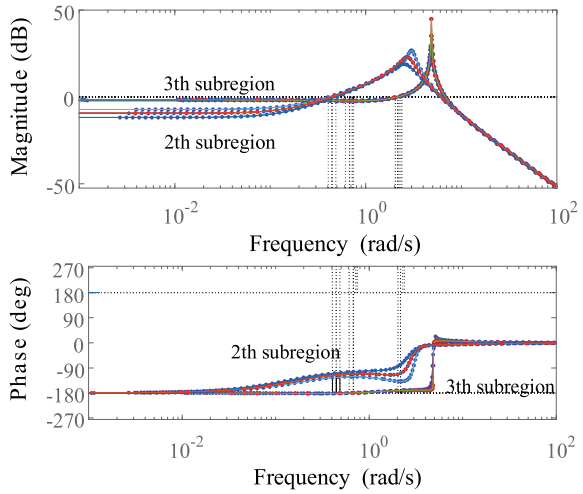

Fig. 5. Bode diagram.

The accuracy requirements in the simulation are that the terminal horizontal displacement and altitude errors are not more than 10m. In addition, the stable region in Theorem 2 is set to $\Omega_{\text{obj}} = [\eta, \zeta, \omega_n]$. The $\eta = -0.5$ represents the maximum real part of eigenvalues, $\zeta = 0.28$ is the minimum damping ratio, and $\omega_n = 16$ denotes the maximum natural frequency.

B. Verification of Aerospace Vehicle LPV Mode

The flight envelope is set to $V \in [400, 850]\text{m/s}$ and $h \in [9000, 12000]\text{m}$, then the flight envelope is evenly divided by $\Delta v = 50\text{m/s}$ and $\Delta h = 100\text{m}$, and 31×10 linear systems are obtained. After many experiments, it is found that when the value of λ is about 0.5, the optimal number of subenvelopes can be acquired, and the dynamic characteristics of linear models in each subenvelope are similar. Here, we set $\lambda = 0.45$. Through Algorithm 1, 30 subenvelopes are finally obtained, and the nominal points in the 30 subenvelopes are determined to establish the LPV model.

Fig. 5 shows the Bode diagram of $\delta_e - \alpha$ of each sampling point in the second and third subregions. Among them, the Bode diagram of a nominal point is a red curve, and the Bode diagrams of other points are set to blue.

From Fig. 5, we can know that the Bode diagram of the nominal point is located in the middle of the envelope, and the systems have different characteristics in different

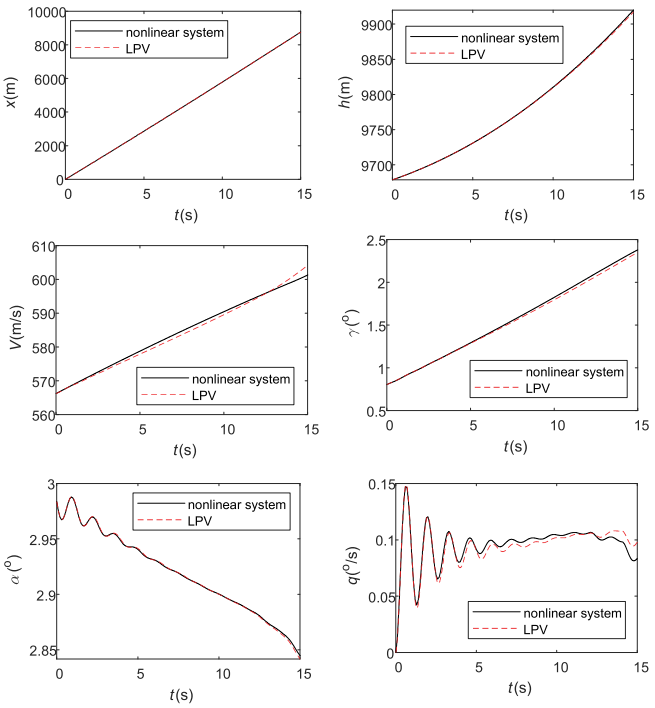

Fig. 6. Time responses for control input.

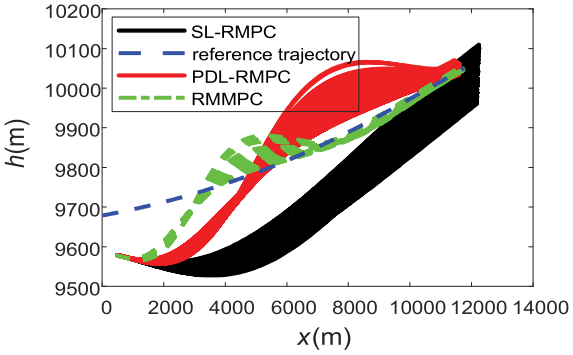

Fig. 7. Monte Carlo simulation with parameter uncertainties and initial error $\boldsymbol{e}_1$.

subregions. Therefore, the selected nominal point is entitled to represent this subregion. Then, an LPV model is built based on these nominal points. In the end, the corresponding polytopic model is derived from Section III-B, taking 30% aerodynamic uncertainty into account.

Next, we will check whether the obtained LPV model of GHAME captures the local nonlinearities of the original system. We take the flight condition $V = 566\text{m/s}$ and $h = 9678\text{m}$ as an example. The control inputs are defined as follows:

$$\delta_e = -0.098\text{rad}, \phi = \begin{cases} 0.82, & 0\text{s} \leqslant t < 3\text{s} \\ 0.75, & 3\text{s} \leqslant t < 17\text{s} \\ 0.99, & t \geqslant 17\text{s}. \end{cases}$$

Fig. 6 shows the time responses of two control inputs for the nonlinear model and the LPV model. From these simulation results, it is observed that the LPV model follows

Authorized licensed use limited to: NANJING UNIVERSITY OF AERONAUTICS AND ASTRONAUTICS. Downloaded on April 15,2022 at 03:18:40 UTC from IEEE Xplore. Restrictions apply.

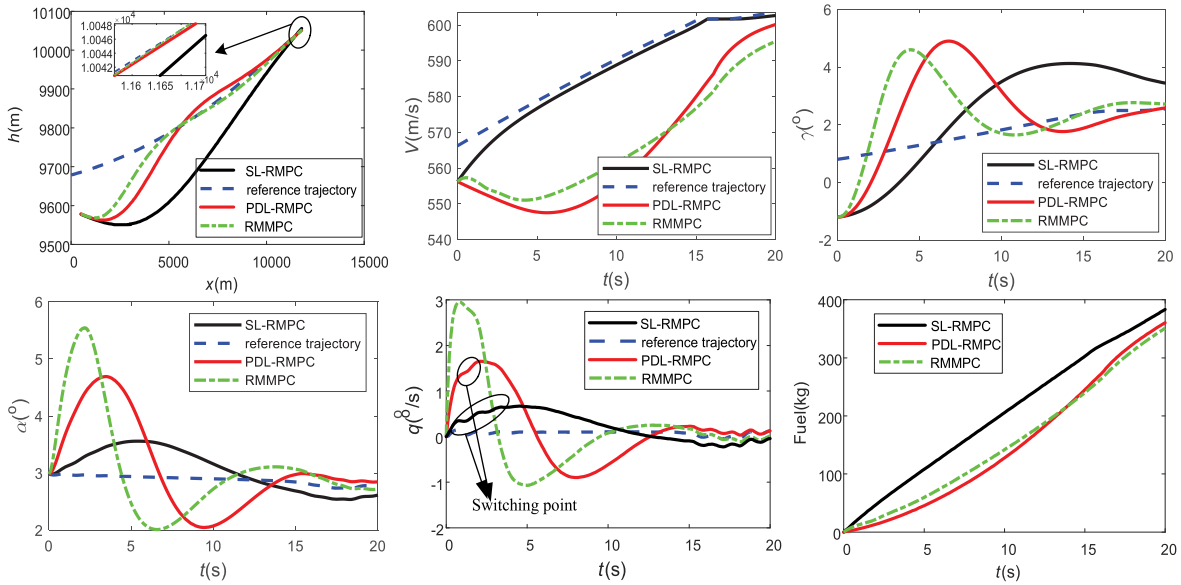

Fig. 8. State curves and fuel consumption with parameter uncertainties and $\boldsymbol{e}_1$.

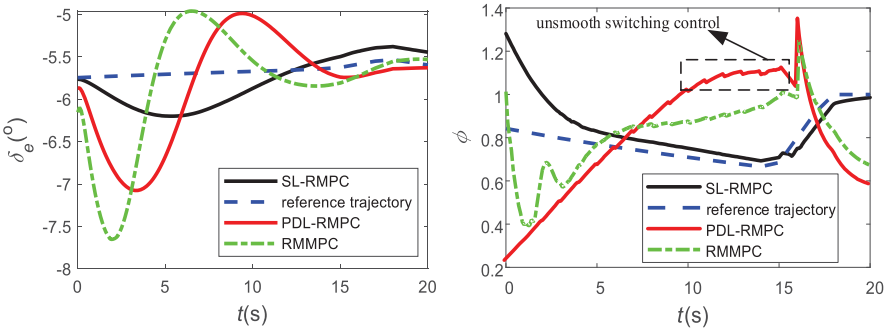

Fig. 9. Control curves with parameter uncertainties and $\boldsymbol{e}_1$.

the nonlinear model quite closely, and we conclude that this model is suitable for the model-based control.

C. Simulation Results and Analysis

Fig. 7 shows the 1000 Monte Carlo simulation results of the SL-RMPC [22], PDL-RMPC [23], and RMMPC for the uncertain ASV system with 30% parameter uncertainty and an initial deviation $\boldsymbol{e}_1 = [500\text{m}, -100\text{m}, -10\text{m/s}, -2^{\text{o}}, 0^{\text{o}}, 0^{\text{o}}/\text{s}]^{\text{T}}$. In addition, the tracking experiments of SL-RMPC, PDL-RMPC, and RMMPC for the ASV system with 30% parameter uncertainty under the initial deviation $\boldsymbol{e}_1$ are exhibited in Fig. 8. Through the batch simulation test, the parameters δ_1 and δ_2 of Algorithm 2 are set to $\delta_1 = 1000$ and $\delta_2 = 10$. Fig. 9 illustrates the control curves given via the aforementioned three control algorithms. In all the simulation diagrams, the reference trajectory is drawn with a dashed blue line.

According to Fig. 7 and the fuel consumption curve in Fig. 8, the RMMPC has stronger robustness and higher accuracy than the SL-RMPC under the uncertainties and initial deviation, and fuel consumption is also lower. Table II shows the single-cycle calculation time and total simulation time of the PDL-RMPC and the RMMPC. From the simulation results shown in Figs. 7 and 8 and Table II, it can be known that the robustness, fuel consumption, and tracking accuracy of the RMMPC strategy are not much different from PDL-RMPC under the initial error $\boldsymbol{e}_1$ and uncertainties. However, the RMMPC strategy can decrease the online calculation, thus improving the calculation efficiency on the basis of ensuring the tracking accuracy.

TABLE II
Computational Efficiency

Algorithms	PDL-RMPC	RMMPC	TRT scheme
Sing cycle calculation time	1.14s	0.23s	0.238s
Total simulation time	49.4s	22.05s	22.25s

In addition, according to the pitch rate change curve in Fig. 8, it can be seen that the RMMPC strategy can guarantee the smooth switching between controllers, thereby improving the smoothness and stability of the flight process. From the control curves of Fig. 9, the control curves are all within the constraint range during the simulation, and

Authorized licensed use limited to: NANJING UNIVERSITY OF AERONAUTICS AND ASTRONAUTICS. Downloaded on April 15,2022 at 03:18:40 UTC from IEEE Xplore. Restrictions apply.

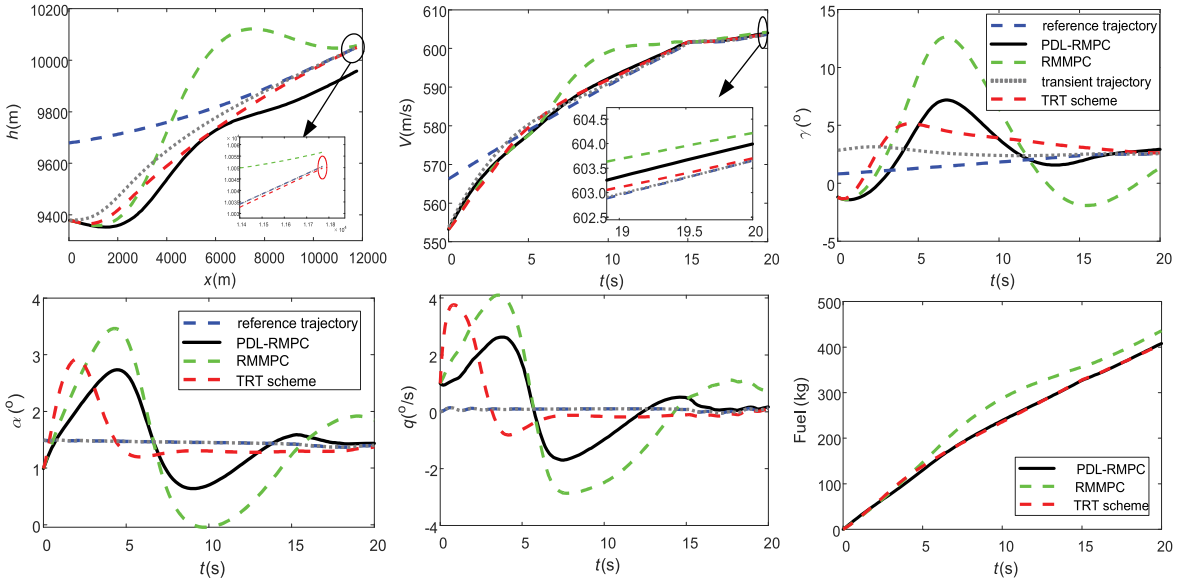

Fig. 10. State curves and fuel consumption with parameter uncertainties and $\boldsymbol{e}_2$.

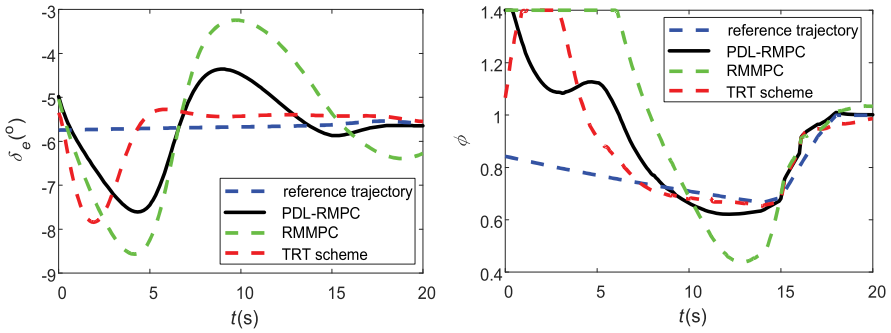

Fig. 11. Control curves with parameter uncertainties and $\boldsymbol{e}_2$.

the control curves obtained by the RMMPC strategy are smoother. Therefore, it can be concluded that the RMMPC can enhance the calculation efficiency on the basis of ensuring the tracking accuracy, and make sure the smooth switching of the transition process.

Next, the range of the initial deviation is further expanded to $\boldsymbol{e}_2 = [30\text{m}, -300\text{m}, -13\text{m/s}, -2^\text{o}, -1^\text{o}, 1^\text{o}/\text{s}]^\text{T}$, and GHAME with 30% parameter uncertainty is considered, then PDL-RMPC, RMMPC strategy, and TRT scheme are used for simulation, respectively. Through extensive simulations, the gains k_1 and k_2 in (66) are chosen as $k_1 = 0.05$ and $k_2 = 0.0978$. Fig. 10 shows the state change curves and fuel consumption during the tracking process. Fig. 11 describes the control curves obtained under the aforementioned algorithms. Among them, the gray point line indicates the transient trajectory.

The red circle in Fig. 10 represents the allowable range of precision, its center is (x_r, h_r) and radius is 10m. From Fig. 10, it can be seen that only the control law obtained by the TRT scheme enables the GHAME to reach the terminal accuracy requirement within 20s. In addition, the PDL-RMPC method obviously cannot achieve target tracking under the initial error $\boldsymbol{e}_2$ (black line in Fig. 10), so this method will not be discussed in the subsequent analysis.

In Figs. 10 and 11, it is found that the RMMP method increases the control energy to quickly eliminate the large initial error. However, this method cannot allocate control energy well during flight (green dotted line in Fig. 11), resulting in an excessive overshoot of state curve (as shown in green dotted line in Fig. 10). According to Fig. 10 and the curve of the FER in Fig. 11, it can be drawn that the TRT scheme reconstructs the tracking command online by the transient trajectory (gray point line) to decompose the excessive initial error $\boldsymbol{e}_2$ along time. Therefore, the TRT scheme can reasonably distribute the control energy with the time range to reduce the actuator saturation and improve the tracking accuracy.

The results in Fig. 10 and Table II demonstrate that the tracking accuracy can be further improved by setting the dynamic transient trajectory; in addition, without excessively increasing the online calculation cost. And Fig. 11 shows that both the elevator deflection and thrust input are kept within a reasonable range.

In addition, Fig. 12 demonstrates the distribution of the closed-loop poles of GHAME during the entire flight with or

Authorized licensed use limited to: NANJING UNIVERSITY OF AERONAUTICS AND ASTRONAUTICS. Downloaded on April 15,2022 at 03:18:40 UTC from IEEE Xplore. Restrictions apply.

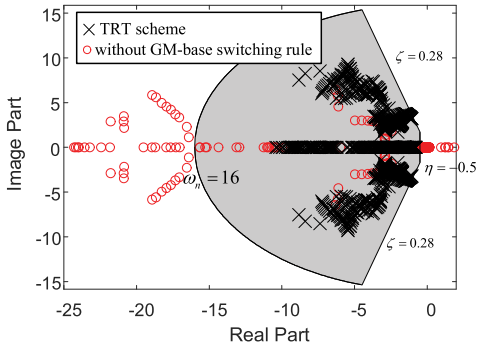

Fig. 12. Closed-loop pole distribution.

without switching strategy. Among them, the one equipped with the switching strategy is our proposed TRT scheme.

It follows from Fig. 12 that if the TRT scheme does not possess this switching strategy, the switching stability between the controllers cannot be assured, resulting in the closed-loop system poles not being all in Ω_{obj}. However, under the TRT scheme, it can be guaranteed that all closed-loop system poles are in Ω_{obj} throughout the flight process. Consequently, the TRT scheme proposed in this article can ensure the smoothness and stability in the flight process and the tracking precision when the ASV has uncertainties and initial deviations.

VI. CONCLUSION

In this article, a TRT scheme is proposed to solve the problems of accurate tracking and rapid response of ASVs, under the uncertainties and initial deviations. This scheme uses the tracking command correction module to adjust the reference trajectory overcoming the actuator saturation problem caused by excessive initial deviation; then it applies the RMMPC strategy to design the controller to automatically regulate the elevator angle and fuel equivalence ratio so that the ASV can track the corrected trajectory.

The simulation results of the nonlinear GHAME model indicate that the TRT scheme possesses the features of fast response, high tracking accuracy, and strong robustness. In addition, these results also show that in the case of large initial error, the TRT scheme can also allocate control energy by adjusting the tracking trajectory online, so as to expand the initial feasible range.

ACKNOWLEDGMENT

The authors would like to thank the editor-in-chief, associate editor and anonymous reviewers for their valuable comments to improve the quality of this paper.

REFERENCES

[1] J. Ding and S. N. Balakrishnan
Intelligent constrained optimal control of aerospace vehicles with model uncertainties
J. Guid., Control, Dyn., vol. 35, no. 5, pp. 1582–1592, Sep. 2012, doi: 10.2514/1.54505.

[2] R. Cao, H. Shen, Y. Liu, and Y. Lu
The LOES-based control scheme of aerospace vehicle under flying quality constraints
Acta Astronautica, vol. 177, pp. 258–269, Dec. 2020, doi: 10.1016/j.actaastro.2020.07.035.

[3] Z. Guo, J. Guo, J. Zhou, and J. Chang
Robust tracking for hypersonic reentry vehicles via disturbance estimation-triggered control
IEEE Trans. Aerosp. Electron. Syst., vol. 56, no. 2, pp. 1279–1289, Dec. 2020, doi: 10.1109/TAES.2019.2928605.

[4] G. H. Wu, X. Y. Meng, and F. Y. Wang
Improved nonlinear dynamic inversion control for a flexible air-breathing hypersonic vehicle
Aerosp. Sci. Technol., vol. 78, pp. 734–743, Jul. 2018, doi: 10.1016/j.ast.2018.04.036.

[5] H. Xu, M. D. Mirmirani, and P. A. Ioannou
Adaptive sliding mode control design for a hypersonic flight vehicle
J. Guid., Control, Dyn., vol. 27, no. 5, pp. 829–838, Sep. 2004, doi: 10.2514/1.12596.

[6] N. T. Nguyen, I. Prodan, and L. Lefèvre
Stability guarantees for translational thrust-propelled vehicles dynamics through NMPC designs
IEEE Trans. Control Syst. Technol., vol. 29, no. 1, pp. 207–219, Jan. 2021, doi: 10.1109/TCST.2020.2974146.

[7] E. Hill, S. A. Gadsden, and M. Biglarbegian
Explicit nonlinear MPC for fault tolerance using interacting multiple models
IEEE Trans. Aerosp. Electron. Syst., vol. 57, no. 5, pp. 2784–2794, Oct. 2021, doi: 10.1109/TAES.2021.3065089.

[8] J. Chai, E. Medagoda, and E. Kayacan
Adaptive and efficient model predictive control for booster reentry
J. Guid., Control, Dyn., vol. 43, no. 12, pp. 2372–2382, Oct. 2020, doi: 10.2514/1.G004925.

[9] X. Hu, L. Wu, C. Hu, and H. Gao
Fuzzy guaranteed cost tracking control for a flexible air-breathing hypersonic vehicle
IET Control Theory Appl., vol. 6, no. 9, pp. 1238–1249, 2012, doi: 10.1049/iet-cta.2011.0065.

[10] Y. Hu, F. Sun, and H. Liu
Neural network-based robust control for hypersonic flight vehicle with uncertainty modelling
Int. J. Model. Identification Control, vol. 11, no. 1/2, pp. 87–98, Sep. 2010, doi: 10.1504/IJMIC.2010.035283.

[11] U. Eren, A. Prach, B. B. Kocer, S. V. Rakovic, E. Kayacan, and B. Acikmese
Model predictive control in aerospace systems: Current state and opportunities
J. Guid., Control, Dyn., vol. 40, no. 7, pp. 1541–1566, Apr. 2017, doi: 10.2514/1.G002507.

[12] S. Mate, H. Kodamana, S. Bhartiya, and P. S. V. Nataraj
A stabilizing sub-optimal model predictive control for quasi-linear parameter varying systems
IEEE Control Syst. Lett., vol. 4, no. 2, pp. 402–407, Apr. 2020, doi: 10.1109/LCSYS.2019.2937921.

[13] A. Casavola, D. Famularo, and G. Franze
A feedback min-max MPC algorithm for LPV systems subject to bounded rates of change of parameters
IEEE Trans. Autom. Control, vol. 47, no. 7, pp. 1147–1153, Jul. 2002, doi: 10.1109/TAC.2002.800662.

[14] M. Soliman, O. P. Malik, and D. T. Westwick
Multiple model predictive control for wind turbines with doubly fed induction generators
IEEE Trans. Sustain. Energy, vol. 2, no. 3, pp. 215–225, Jul. 2011, doi: 10.1109/TSTE.2011.2153217.

[15] L. Wu, X. Yang, and F. Li
Nonfragile output tracking control of hypersonic air-breathing vehicles with an LPV model
IEEE/ASME Trans. Mechatronics, vol. 18, no. 4, pp. 1280–1288, Aug. 2013, doi: 10.1109/TMECH.2013.2255064.

Authorized licensed use limited to: NANJING UNIVERSITY OF AERONAUTICS AND ASTRONAUTICS. Downloaded on April 15,2022 at 03:18:40 UTC from IEEE Xplore. Restrictions apply.

[16] X. Tao, N. Li, and S. Li
Multiple model predictive control for large envelope flight of hypersonic vehicle systems
Inf. Sci., vol. 328, pp. 115–126, Jan. 2016, doi: 10.1016/j.ins.2015.08.033.

[17] L. Teng, Y. Wang, W. Cai, and H. Li
Robust fuzzy model predictive control of discrete-time Takagi-Sugeno systems with nonlinear local models
IEEE Trans. Fuzzy Syst., vol. 26, no. 5, pp. 2915–2925, Oct. 2018, doi: 10.1109/TFUZZ.2018.2815521.

[18] Y. Liang, Y. Li, A. Khajepour, and L. Zheng
Holistic adaptive multi-model predictive control for the path following of 4WID autonomous vehicles
IEEE Trans. Veh. Technol., vol. 70, no. 1, pp. 69–81, Jan. 2021, doi: 10.1109/TVT.2020.3046052.

[19] L. Cavanini, G. Ippoliti, and E. F. Camacho
Model predictive control for a linear parameter varying model of an UAV
J. Intell. Robot Syst., vol. 101, no. 57, pp. 1–18, Mar. 2021, doi: 10.1007/s10846-021-01337-x.

[20] Y. Yu, J. Sun, H. Liu, P. Zhu, and Q. Ye
Reactor temperature control system based on multi-model predictive control
Proc. Int. Conf. Nucl. Eng., vol. 27, Dec. 2019, Art. no. 1160, doi: 10.1299/jsmeicone.2019.27.1160.

[21] H. A. Pipino, C. A. Cappelletti, and E. J. Adam
Adaptive multi-model predictive control applied to continuous stirred tank reactor
Comput. Chem. Eng., vol. 145, pp. 1–11, Feb. 2021, doi: 10.1016/j.compchemeng.2020.107195.

[22] Y. I. Lee, M. Cannon, and B. Kouvaritakis
Extended invariance and its use in model predictive control
Automatica, vol. 41, no. 12, pp. 2163–2169, Dec. 2005, doi: 10.1016/j.automatica.2005.07.012.

[23] F. A. Cuzzola, J. C. Geromel, and M. Morari
An improved approach for constrained robust model predictive control
Automatica, vol. 38, no. 7, pp. 1183–1189, Jul. 2002, doi: 10.1016/S0005-1098(02)00012-2.

[24] R. Colgren, S. Keshmiri, and M. Mirmirani
Nonlinear ten-degree-of-freedom dynamics model of a generic hypersonic vehicle
J. Aircr., vol. 46, no. 3, pp. 800–813, May 2009, doi: 10.2514/1.35644.

[25] P. Vu and D. J. Biezad
Direct-lift design strategy for longitudinal control of hypersonic aircraft
J. Guid., Control, Dyn., vol. 17, no. 6, pp. 1260–1266, Nov. 1994, doi: 10.2514/3.21342.

[26] J. M. Oscar
A fast ascent trajectory optimization method for hypersonic air-breathing vehicles
Ph.D. dissertation, Iowa State University, Ames, IA, USA, Aug. 2010.

[27] B. Agus
An approach to the use of neural network in the analysis of a class of flight vehicles
Ph.D. dissertation, Massachusetts Institute of Technology, Cambridge,, MA, USA, Jan. 2010.

[28] T. Koenings, M. Krueger, H. Luo, and S. X. Ding
A data-driven computation method for the gap metric and the optimal stability margin
IEEE Trans. Autom. Control, vol. 63, no. 3, pp. 805–810, Mar. 2018, doi: 10.1109/TAC.2017.2735023.

[29] Y. Li, Y. Wu, and X. Qu
Chicken swarm-based method for ascent trajectory optimization of hypersonic vehicles
J. Aerosp. Eng., vol. 30, no. 5, pp. 40–43, Sep. 2017, doi: 10.1061/(ASCE)AS.1943-5525.0000757.

[30] A. Brown and D. Anderson
Trajectory optimization for high-altitude long-endurance UAV maritime radar surveillance
IEEE Trans. Aerosp. Electron. Syst., vol. 56, no. 3, pp. 2406–2421, Jun. 2020, doi: 10.1109/TAES.2019.2949384.

[31] G. Tang, F. Jiang, and J. Li
Fuel-optimal low-thrust trajectory optimization using indirect method and successive convex programming
IEEE Trans. Aerosp. Electron. Syst., vol. 54, no. 4, pp. 2053–2066, Aug. 2018, doi: 10.1109/TAES.2018.2803558.

[32] R. Chai, A. Savvaris, and A. Tsourdos
Violation learning differential evolution-based hp-adaptive pseudospectral method for trajectory optimization of space maneuver vehicle
IEEE Trans. Aerosp. Electron. Syst., vol. 53, no. 4, pp. 2031–2044, Aug. 2017, doi: 10.1109/TAES.2017.2680698.

[33] T. Guo, J. Li, H. Baoyin, and F. Jiang
Pseudospectral methods for trajectory optimization with interior point constraints: Verification and applications
IEEE Trans. Aerosp. Electron. Syst., vol. 49, no. 3, pp. 2005–2017, Jul. 2013, doi: 10.1109/TAES.2013.6558034.

[34] L. Yi
Tensor product space ANOVA models
Ann. Statist., vol. 28, no. 3, pp. 734–755, Jun. 2000, doi: 10.1214/aos/1015951996.

[35] W. Kwon and A. Pearson
On feedback stabilization of time-varying discrete linear systems
IEEE Trans. Autom. Control, vol. 23, no. 3, pp. 479–481, Jun. 1978, doi: 10.1109/TAC.1978.1101749.

[36] M. C. Oliveira, J. Bernussou, and J. C. Geromel
A new discrete-time robust stability condition
Syst. Control Lett., vol. 37, no. 4, pp. 261–265, Jul. 1999, doi: 10.1016/S0167-6911(99)00035-3.

[37] L. Saydy, A. L. Tits, and E. H. Abed
Guardian maps and the generalized stability of parametrized families of matrices and polynomials
Math. Control Signals Syst., vol. 3, no. 4, pp. 345–371, Dec. 1990, doi: 10.1007/BF02551375.

[38] U. Mackenroth
Robust Control Systems Theory and Case Studies. Berlin, Germany: Springer, 2004, pp. 289–309.

[39] D. Xiao, M. Liu, Y. Liu, and Y. Lu
Switching control of a hypersonic vehicle based on guardian maps
Acta Astronautica, vol. 122, pp. 294–306, May 2016, doi: 10.1016/j.actaastro.2016.02.017.

[40] K.-Y. Wang, A. M.-C. So, T.-H. Chang, W.-K. Ma, and C.-Y. Chi
Outage constrained robust transmit optimization for multiuser MISO downlinks: Tractable approximations by conic optimization
IEEE Trans. Signal Process., vol. 62, no. 21, pp. 5690–5705, Nov. 2014, doi: 10.1109/TSP.2014.2354312.

[41] H. Bloemen, T. Boom, and H. Verbruggen
Optimizing the end-point state-weighting matrix in model-based predictive control
Automatica, vol. 38, no. 6, pp. 1061–1068, Jun. 2002, doi: 10.1016/S0005-1098(01)00296-5.

[42] Z. He, D. Li, and Y. Lu
Disturbance compensation based piecewise linear control design for perching maneuvers
IEEE Trans. Aerosp. Electron. Syst., vol. 55, no. 1, pp. 192–204, Jun. 2019, doi: 10.1109/TAES.2018.2849898.

Authorized licensed use limited to: NANJING UNIVERSITY OF AERONAUTICS AND ASTRONAUTICS. Downloaded on April 15,2022 at 03:18:40 UTC from IEEE Xplore. Restrictions apply.

Rui Cao was born in Shangqiu, Henan, China, in 1994. She is currently working toward the Ph.D. degree in navigation, guidance, and control.

Her research interests include control design, trajectory optimization, and system identification.

Yanbin Liu was born in Hunan, Sichuang Province, China, in 1980. He received the B.S. and Ph.D. degrees in navigation, guidance, and control from the Nanjing University of Aeronautics and Astronautics, Nanjing, China, in 2002 and 2007, respectively.

He is currently an Associate Professor with the College of Astronautics, Nanjing University of Aeronautics and Astronautics. His research interests include hypersonic vehicle control and complex modeling and control of vehicle.

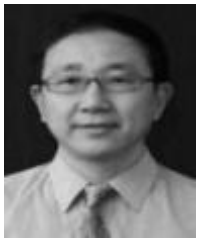

Yuping Lu received the B.S. degree in navigation, guidance, and control from the Nanjing University of Aeronautics and Astronautics, Nanjing, China.

From 1992 to 1994, he was a Visiting Scholar with the University of Supelec, Gif-sur-Yvette, France. From 2000 to 2001, he was a Senior Visiting Scholar with the University of Rennes, Rennes, France. He is currently a Full Professor with the College of Automation Engineering, Nanjing University of Aeronautics and Astronautics. His primary research interests include hypersonic vehicle control, network, and remote control technology.

Authorized licensed use limited to: NANJING UNIVERSITY OF AERONAUTICS AND ASTRONAUTICS. Downloaded on April 15,2022 at 03:18:40 UTC from IEEE Xplore. Restrictions apply.